



# Synthesis of a superhydrophobic self-cleaning coating through dual-scale carbon sphere based colloidal assembly

Thomas O'Connor

## Publication date

01-01-2012

## Licence

This work is made available under the [CC BY-NC-SA 1.0](#) licence and should only be used in accordance with that licence. For more information on the specific terms, consult the repository record for this item.

## Document Version

1

## Citation for this work (HarvardUL)

O'Connor, T. (2012) 'Synthesis of a superhydrophobic self-cleaning coating through dual-scale carbon sphere based colloidal assembly', available: <https://hdl.handle.net/10344/2861> [accessed 25 Feb 2023].

This work was downloaded from the University of Limerick research repository.

For more information on this work, the University of Limerick research repository or to report an issue, you can contact the repository administrators at [ir@ul.ie](mailto:ir@ul.ie). If you feel that this work breaches copyright, please provide details and we will remove access to the work immediately while we investigate your claim.



UNIVERSITY of LIMERICK

O L L S C O I L L U I M N I G H

# Synthesis of a Superhydrophobic Self-Cleaning Coating through Dual-Scale Carbon Sphere based Colloidal Assembly

Department of Chemical and Environmental Sciences,  
University of Limerick

Thomas O'Connor

Supervisor: Dr. Kevin M. Ryan

Submitted to the University of Limerick for the  
Degree of Masters of Science

September 2012

## Declaration

This project is a presentation of my original research work. Wherever contributions of others are involved, every effort is made to indicate this clearly, with due reference to the literature, and acknowledgments of collaborative research and discussions. The work was done under the guidance of Dr. Kevin M Ryan from the Chemical and Environmental Science Department at the University of Limerick.

---

Thomas O'Connor

## **Acknowledgements**

I would like to thank Dr. Kevin Ryan for his support and guidance throughout the course of this project. I would also like to thank my entire research group for their support and help throughout the year.

## Abstract

Superhydrophobicity can be seen in nature with varying degrees of wetting. The leaves of the lotus plant have long been identified for their superhydrophobic properties. Superhydrophobic surfaces have contact angles larger than  $150^\circ$  and their sliding angles are less than  $10^\circ$ . Herein we describe how, with the use of evaporated metals, the hydrophobicity of carbon spheres which are intrinsically hydrophobic can be altered to biomimic different states of wetting as seen in nature to create a superhydrophobic self-cleaning coating. Superhydrophobicity was displayed through the determination of contact angle and contact angle hysteresis. Dual-scale roughness was utilised to create the superhydrophobic coating with surface structure playing a vital role in its creation.

## Table of Contents

1	Introduction .....	7
1.1	Background .....	7
1.2	Examples in Nature .....	17
1.2.1	Hydrophobicity and the Water Strider .....	18
1.2.2	Butterfly Wings and Hysteresis .....	19
1.2.3	Pinning of Water and the Red Rose .....	21
1.2.4	Superhydrophobicity and the Lotus Leaf .....	22
1.3	Applications .....	26
1.4	Methods for the Preparation of Superhydrophobic Surfaces .....	32
1.4.1	Polymer Materials .....	32
1.4.2	Electrospinning .....	34
1.4.3	Chemical Vapor Deposition (CVD) .....	34
1.4.4	Etching and Lithography .....	36
1.4.5	Physical Vapour Deposition (PVD) .....	37
1.4.6	Layer-by-Layer and colloidal Assembly .....	41
1.4.7	Growth of particles .....	43
1.5	Supercritical Carbon Dioxide .....	45
2	Characterisation Techniques .....	48
2.1	Scanning Electron Microscope .....	48
2.2	Contact Angle Meter .....	52

2.3	Contact Angle Hysteresis .....	54
3	Experimental .....	56
3.1	Supercritical Carbon Dioxide Nanoparticle Formation.....	57
3.2	Metal Evaporation .....	58
3.3	Contact Angle.....	59
4	Results and Discussion.....	61
4.1.1	Temperature Programme .....	62
4.1.2	Effect of Temperature on the System .....	64
4.1.3	Effect of Pressure on the System .....	66
4.1.4	Squalane Injection Volume Study .....	67
4.1.5	Summary of Optimisation .....	68
4.1.6	Contact Angle of Carbon Spheres .....	69
4.1.7	Contact Angle Hysteresis of Carbon Spheres.....	70
4.2	Roughening of the Carbon Spheres.....	73
4.2.6	Evaporated Titanium.....	73
4.2.7	Evaporated Aluminium.....	75
4.2.8	Evaporated Indium.....	77
4.3	Contact Angle Hysteresis of 20nm Evaporated Indium Layer.....	82
4.4	Self-Cleaning Properties.....	85
5.	Conclusion .....	88
6.	Future Work .....	90

7	References .....	92
---	------------------	----



# 1 Introduction

## 1.1 Background

It may be easily mistaken that with current progress in science and technology that advances in this field have far surpassed that seen in nature. The fact is however due to the process of evolution, a great deal of effort is placed on mimicking natural phenomena through synthetic means to replicate the broad and varied “tricks” that nature has obtained over time. There are many examples of this biomimicry, with one of the most simplest and famous being the invention of Velcro seen with a Swiss mountaineer/inventor and his dog. When he saw the burs of plants clinging to his dog’s fur, and with the aid of his microscope, he concluded that the hooks in the burs allowed the burr to fasten tightly to the loops in the fur of the dog to transport the seeds inside. It was thus this hook and loop idea which spurred the invention of Velcro<sup>1</sup>. Another example which has gained much scientific interest in recent years is that of the water repellency of plants and animals, in particular that of the lotus leaf. The leaf of the lotus repels water so strongly that water “beads up” on the surface and rolls off with minimal tilting<sup>2</sup>. This strong repellency allows the leaf to remove dirt or dust particles on the surface of the plant as the water particles roll off the surface. It is therefore this principle effect of “self-cleaning” that makes the properties of the lotus such an interesting and desirable characteristic.

Although water repellency has been investigated for several decades, it has only been recently that the term hydrophobicity has appeared in literature. Great effort has been made in harmonising the language used to describe the wetting of materials. It is therefore generally accepted in literature that if the liquid wets the surface

(hydrophilic surface), the value of the contact angle is  $0 \leq \theta \leq 90^\circ$ , whereas if the liquid does not wet the surface (hydrophobic surface), the value of the contact angle should be  $90^\circ < \theta \leq 180^\circ$ . From this a classification of superhydrophobicity has emerged. This classification is used to describe surfaces which display a self-cleaning or “rolling ball” effect with water. It is generally accepted that a surface is superhydrophobic if it has a water contact angle above  $150^\circ$ , with contact angle hysteresis below  $10^\circ$ . This information is summarised in Table 1.1 below.

**Table 1.1** *Summary of ranges of contact angle and their classification with examples of each.*

Contact Angle ( $^\circ$ )	Classification	Example
<b>~0</b>	Super-hydrophilic	UV irradiated $\text{TiO}_2$
<b>&lt;90</b>	Hydrophilic	Glass
<b>90-149</b>	Hydrophobic	Teflon
<b>150-180</b>	Super-hydrophobic	Lotus Leaf

The study of the wetting of materials is not new, with the idea of wetting long been studied and philosophised over with Aristotle, Archimedes, and Galileo all having theories as to the wetting of materials and their contact with water. The modern theory on wetting and contact angle between two materials is accredited to Thomas Young and Pierre Simon de Laplace, with the Young-Laplace equation (Equation 1) with their work on the adhesion and cohesion at interfaces.<sup>3</sup> Young’s equation relates the contact angle ( $\theta$ ) to three interfacial surface energies involved in the formation of a liquid drop on the surface of a material. The surface energies involved are the solid-vapour ( $\gamma_{SV}$ ), liquid-vapour ( $\gamma_{LV}$ ), and solid-liquid ( $\gamma_{SL}$ ) and are depicted in Figure 1.1. The equation describes how liquids with high surface

tension (high  $\gamma_{LV}$ ) such as water, “beads up” on hydrocarbon surfaces which have a low surface energy (low  $\gamma_{SV}$ ), and how materials with high surface energy (high  $\gamma_{SV}$ ) such as metals cause liquids with high surface tension (high  $\gamma_{LV}$ ) to spread and wet the surface of the material. The relationship between these surface energies and the angle of contact a liquid will make with that material can thus be theoretically calculated. The angle between the surface of the material being measured and the water meniscus at the three phase contact line gives a value of the wetting of the surface  $\theta$ .

$$\cos \theta = \frac{\gamma_{SV} - \gamma_{SL}}{\gamma_{LV}} \quad \text{Eq. 1}$$

Young’s equation therefore shows that chemical composition<sup>4, 5</sup> determine the surface free energy and thus has great influence on wettability. It can be seen that a surface with a large surface energy will almost completely wet the surface approaching a contact angle of  $\theta = 0^\circ$ , where if the material at the solid gas interface has a low surface energy the contact angle can theoretically approach  $180^\circ$ , this however has certain limitations.

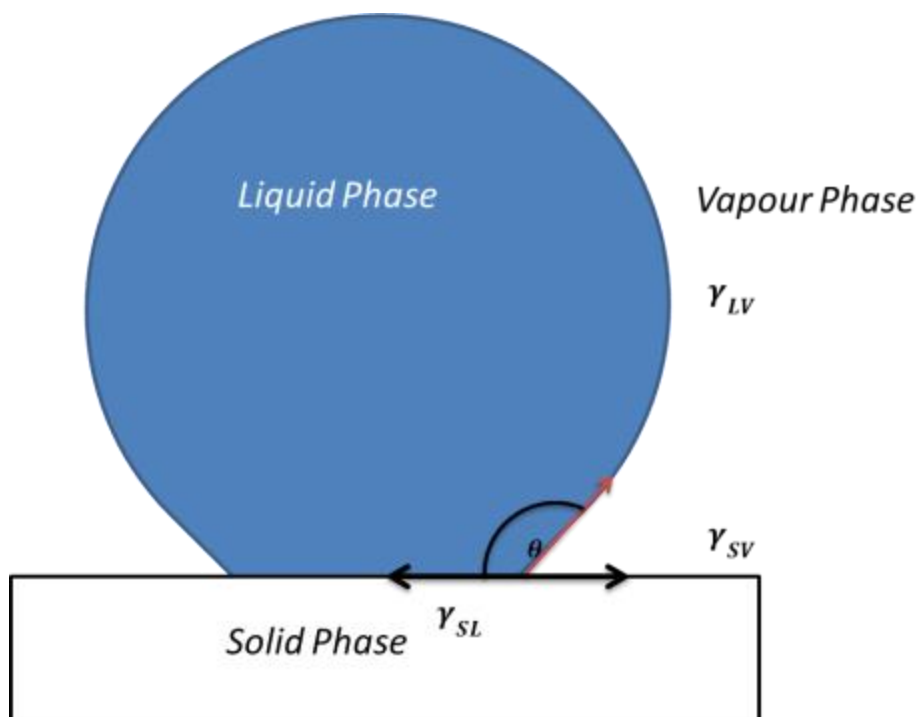


**Figure 1.1** An illustration of the relationship between the surface and interface tension according to Young's equation.

The  $-\text{CF}_3$ -terminated surface was reported to possess the lowest surface free energy available in any material. According to Young's Equation this material would be the most likely material to create a contact angle with water approaching  $180^\circ$ , displaying superhydrophobicity on a smooth surface. It has been shown however that the maximum C.A achieved with this  $-\text{CF}_3$ -terminated material could only reach a water contact angle of about  $120^\circ$ .<sup>6</sup> This contact angle for an extremely low surface free energy fluorinated material on a smooth surface suggests that in order to achieve high contact angles approaching  $180^\circ$ , other factors must be accounted for in order to achieve superhydrophobic wetting states.

It was not until the work of Wenzel<sup>7</sup> in 1936 and then Cassie-Baxter<sup>8</sup> in 1944 that the idea that a roughened surface increases the hydrophobicity of a material was proposed. Wenzel suggested that if a sessile drop of water was placed on a rough surface, then the roughness of the surface should either emphasise the

intrinsic wetting tendency of the drop towards either greater hydrophobicity or hydrophilicity depending on the properties of the material and the drop being placed on it as seen in Young's equation. From this, Wenzel saw that the drop formed a circular three phase contact line (solid-vapour, liquid-vapour, and solid-liquid). It was seen that this triphasic line continued to increase in size until the liquid had spread over the surface, or that when the droplet is formed the three phase contact line advances to a certain size and then stops, forming a sessile drop in the shape of a portion of a sphere with the contact angle being produced depending on the chemical composition and topography of the material, and of the drop. From these observations the contact angle observed on these rough surfaces is given by Wenzel's equation (Equation 2),

$$\cos\theta^W = \frac{r(\gamma_{SV} - \gamma_{SL})}{\gamma_{LV}} = r\cos\theta \quad \text{Eq. 2}$$

where  $r$  is the roughness factor of the surface defined as the ratio of the actual area of a rough surface to the geometric projected area. This suggests that the surface free energy of the rough material will be  $r$  times greater than that of a smooth surface of the same material per unit area. This equation shows a linear relationship between roughness and contact angle for a homogeneous material and is useful in explaining the phenomenon of superhydrophobicity. Like the work of Young, certain limitations also apply to Wenzel's work with the roughness factor only seen to be linear up to  $r = 1.7$ , from where a transition within the wetting behaviour of the liquid can be seen.

With specific structuring of the surface, for example Figure 1.2, it can be energetically favourable for the droplet of water to bridge across the features of the material that induce the roughness effect. In this regime of wetting known as the Cassie state or Cassie-Baxter state the drop sits on a composite layer of both the tip of the rough features and the air that rests between these features (Figure 1.3 b). Young's equation was thus further modified to incorporate the idea of Cassie and Baxter. The composite surface was theoretically broken into two fractions in contact with the drop. The sum of the individual contact angles was taken as the contact angle with a unit area of the surface having a surface area fraction  $f_1$  with a contact angle  $\theta_1$  and an area fraction  $f_2$  with a contact angle  $\theta_2$ , the contact angle on the surface can be expressed by the following equation.<sup>9</sup>

$$\cos\theta' = f_1 \cos\theta_1 + f_2 \cos\theta_2 \quad \text{Eq. 3}$$

$$\text{Where } f_1 + f_2 = 1$$

From this it is therefore suggested that any additional surface roughness will impact on the contact angle produced with hydrophobic surfaces (contact angles greater than  $90^\circ$ ) always increasing and those less than  $90^\circ$  potentially moving in either direction. It has been found that controlling the size and shape of the rough asperities on the surface of the material is critical to the support of a large contact angle droplet on the surface. It has been determined that the height of the asperities (H) should be large enough to support droplets from penetrating through with the

smaller nanoscale asperities reducing the contact area and preventing the formation of condensation droplets from within the material.

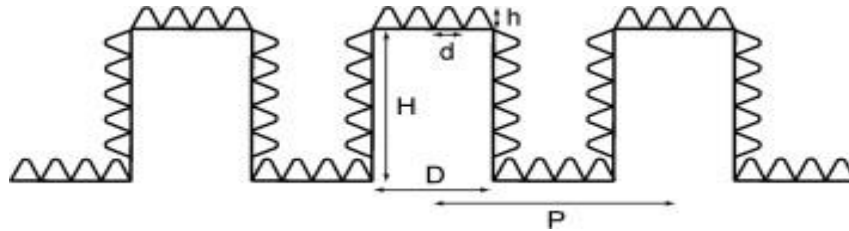


**Figure 1.2** Ideal surface roughness of a superhydrophobic material.

Depending on the surface topography and conditions which arise during the formation of a drop on the surface of a material different wetting states can occur. Figure 1.3 below depicts the different pinning states possible when a drop of water comes in contact with a hydrophobic surface. The Wenzel state of wetting shows that the water penetrates into the space between the features of the rough surface. This increases the surface area in contact with the water droplet and from Wenzel's equation this roughness will theoretically increase the contact angle of the liquid drop with the surface. The drop will however be pinned to the surface of the material due to the large area of contact with the material and any capillary forces that may apply within the features. This state of roughness is more common in nature with many plants and animals possessing microscopic rough features on their surface which aid in de-wetting.<sup>10-12</sup> Figure 1.3 b) depicts the formation of a Cassie-Baxter droplet on the surface of a material. The water droplet rests on the crenels of the surface with air supporting the drop between each crenel. This dramatically reduces the surface in contact with the material, reducing the adhesion of the drop to the surface and thus increasing the ability of the drop to roll with little applied force as

explained by Baxter. Depending on the size and shape of the water and its surface free energy, an intermediate state of wetting can also occur. This intermediate stage can occur when the distance between the asperities is too large and it is not energetically favourable for the water to completely bridge the gap. As the water front recedes within the space, the contact area increases with an equilibrium formed. This state of wetting is most likely to collapse into a Wenzel state with increased velocity of the drop or applied force on the surface of the drop. Water droplets adhere to the surface of Wenzel type surfaces up until a critical volume of liquid is reached where gravitational forces exceed that of the surface energy of the liquid and the surface.

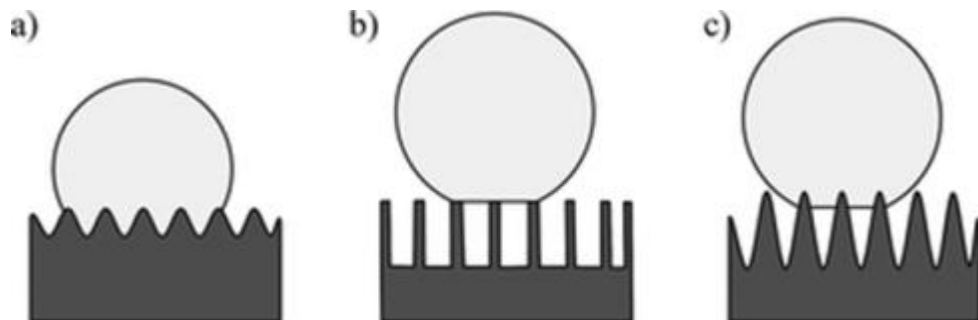


**Figure 1.3** Wetting states (a) Wenzel, (b) Cassie–Baxter and (c) combined models.

Although the use of Young, Wenzel and Cassie-Baxter equations have been cited in many articles, there is some debate as to the validity of these equations. It is suggested and has been demonstrated that these equations do not hold up under specific criteria and was first brought to light by Pease<sup>13</sup> who first argued the validity of Young's equation for determining contact angles. This point was thus further strengthened by the work of Bartell<sup>14</sup> who showed that a surface with a roughness within the three phase contact line and a smooth surface of the same material,



display similar contact angles. This contradicts Wenzel's theory that roughness per unit area on the surface directly increases contact angle. This point has also been further strengthened,<sup>2, 15, 16</sup> particularly by Gao<sup>17</sup> who directly set out to show that the Wenzel and Cassie models do not apply to all roughened surfaces and that the traditional thinking behind the wetting of a material is misplaced. For Wenzel and Cassie's models it is taken that the unit area  $\text{erg/cm}^2$  (energy per unit area) in contact with the liquid is responsible for the contact angle created. Gao suggests that this is incorrect and that the alternative measurement of units  $\gamma$  in equation 1,  $\text{dyn/cm}$  (force per length) is the correct thinking of surface energy and interaction of a surface with its wetting liquid. The idea that force per length is a more accurate description of contact angle was shown through experiments and was determined by interactions of the liquid and the solid at the three-phase contact line alone. It was found that the interfacial area within the contact perimeter was irrelevant to the contact angle formed at the three phase contact line. Since Wenzel and Cassie both deal with the area under the drop to determine contact angle through increased surface area and solid fractions respectively,  $\text{erg/cm}^2$  (energy per unit area) must be used to determine contact angle. The contradiction of both Wenzel and Cassie's regimes can be seen in Figure 1.4 below. Both Wenzel and Cassie's equation respectively would suggest an increase in contact angle seen on these surfaces in contact with water. From practical analysis of these materials it was seen that the dramatic change on the surface within the drop had no effect on contact angle and that the surface energy of the material at the three phase contact line with respect to force per length only affected contact angle and not force per unit area as suggested.



**Figure 1.4** Different topography a) and surface chemistry c) (hydrophilic spot within a hydrophobic material) within a sessile drop which display the same contact angle as a smooth surface of the same material in b).<sup>17</sup>

Although the results of this analysis suggests that the use of the Wenzel and Cassie's equations is void, it has been stated by Milne<sup>18</sup> that with the correct unsimplified form of the Cassie-Baxter equation that the correct contact angle can be calculated through proper determination of the solid/liquid fraction. It is also seen that only in these circumstances where the interior surface of the drop is dramatically different from that of the surface of the material at the three phase contact line will a dramatic difference between the theoretical and measured contact angles be seen. The demonstration of the behaviour of the three phase line on a heterogeneous structure therefore demonstrates that the contact angle determined on these structures are an estimation of the contact angle of the material dependent on the homogeneity of the material being measured and thus its composition with the exterior boundary of the drop.

## 1.2 Examples in Nature

In order to benefit from surface roughness, academia has turned to nature for the answer to superhydrophobicity. Surface texturing and the resultant water repellency are clearly evident in nature. With the increased use and resolution achievable in microscopy since the 1950's, especially that of electron microscopy, surface features within the nanoscale is now evident on flora and fauna which display remarkable hydrophobicity<sup>19</sup>. It was from this that much advancement in the area of fluid manipulation on surfaces is seen, not only in the control of the wetting and non-wetting of water but also ice prevention and the control of non-polar fluids.

Examples in nature of hydrophobicity in flora and fauna are varied in both structure and characteristics. It can be seen in species of bugs and insects such as the *Microveli*<sup>12</sup> and in many birds and animals especially those aquatic in nature<sup>20</sup>. The one common trait in nature is that of micro- and nano-structuring on their surface, such animals and plants can utilise water to their benefit. Below are some examples of controlled wetting as seen in nature and how individual structuring affects wetting. From these structures much of what is currently known about the wetting behaviour of materials can be learned. Due to the diverse array of structures evident in nature, it is possible to demonstrate how the difference in these structures affects the wetting on the surface from pinning and hysteresis to superhydrophobicity. Nature displays many shapes and sizes of both macro- and nano-structuring and learning from these; synthetic materials can be fabricated, mimicking the hydrophobicity seen with such structures.

### 1.2.1 Hydrophobicity and the Water Strider

An interesting example of hydrophobicity seen in nature is that of the legs of the water strider (*Gerris remigis*). It was previously thought that it's capability to effortlessly glide across a water's surface was due to the secretion of a wax<sup>21</sup>, and the curvature of the striders legs<sup>22</sup>. It was seen by Feng<sup>23</sup> and Gao<sup>23, 24</sup> however that the remarkable hydrophobicity of the striders legs was in fact due to the nano-structuring of the legs (Figure 1.5 b and c), with each leg capable of supporting up to fifteen times the weight of the insect.

The structure contains needle like setae. With further investigation of these

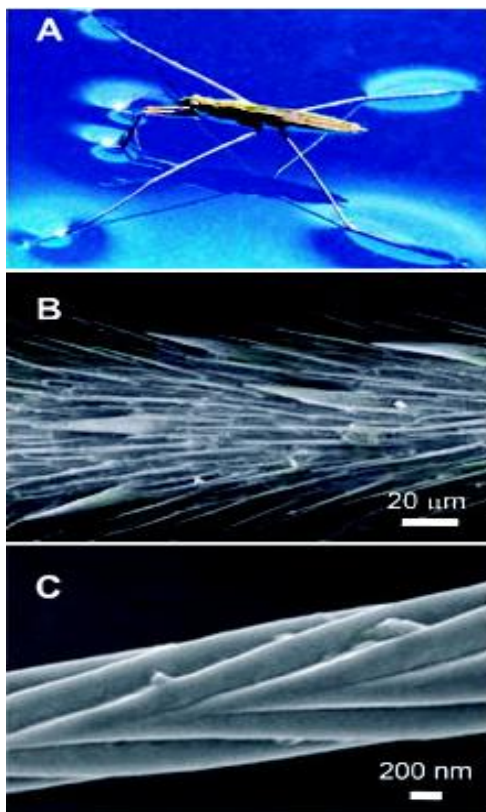


**Figure 1.5** a) Water strider resting on water. b) SEM images of a water strider leg covered by numerous oriented needle-shaped microsetae. c) SEM image of grooved nanostructure on the seta surface.

setae it can be seen that each setae are decorated with nanoscale grooves which give the legs a hierarchical dual scale roughness. It has been shown that the legs of the water strider have a static contact angle with water of up to  $167^\circ$ , one of the largest contact angles seen in nature. It is this dual scale hierarchical roughness that is the common factor that is seen across almost all superhydrophobic surfaces, both natural and synthetic. The needle like structure of the leg allows for a reduction in contact area with the impinging water surface. The replication of this needle

type structure has been synthetically produced, with increased water contact angle as compared to a pillar type structure as seen in lithographic techniques.<sup>25</sup>

### 1.2.2 Butterfly Wings and Hysteresis

Another interesting micro- and nano-structuring in nature which facilitates directional adhesion of water droplets can be seen on the wings of the butterfly *Morpho aega*. The structure of the wing allows water to roll off and away from the body as the insect flies in wet conditions, while inhibiting the drop from rolling onto the body as the wings is pointed upwards during the cycle of the wing in flight. Figure 1.6 shows how the nanometre tips on the edge of the butterfly wings pins the drop of water to the surface in one direction but allows the drop to roll off the surface as the direction of tilt is inverted. The principle of this directional adhesion is currently receiving large interest in the area of microfluidics and lab on a chip technology.<sup>26</sup>

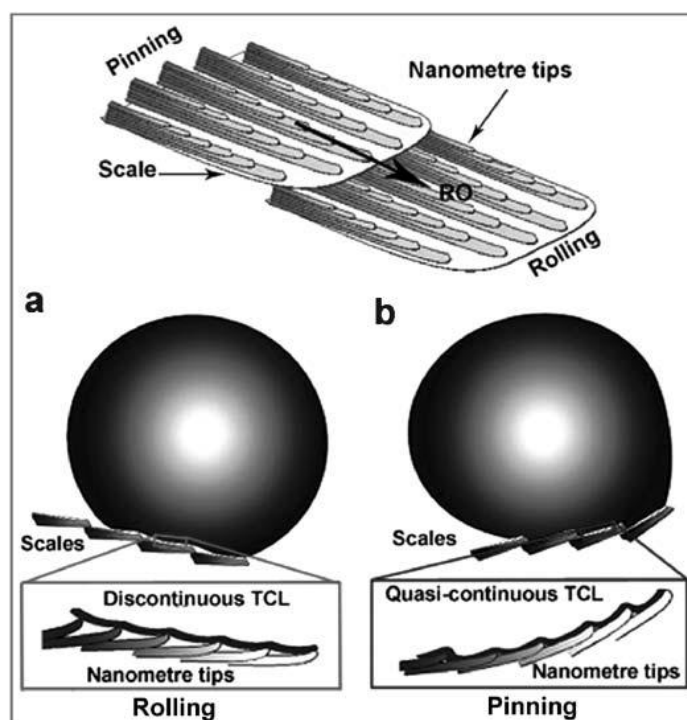


**Figure 1.6** The pinning and rolling effect of water during the flight of the *Morpho aega* butterfly<sup>27</sup>

The large difference in contact angle between the advancing ( $\theta_a$ ) and receding ( $\theta_r$ ) contact angles is known as contact angle hysteresis. This high intrinsic contact angle hysteresis shows a combined Cassie-Baxter/ Wenzel state depending on the direction of the rolling direction. Hysteresis occurs due to the variable “metastable” states which can occur along the three phase contact line.<sup>15, 28</sup> Due to the fact that there are energy barriers which exist between these metastable states, a true “equilibrium” contact angle is impossible to measure in real time. For an ideal surface that is wet by a liquid, contact angle theory predicts one and only one thermodynamically stable contact angle. In practise, however, this ideal surface is rarely found. To fully characterize any surface, therefore, it is important to measure both advancing and receding contact angles and report the difference as the contact angle hysteresis. It is well established that a high contact angle is not sufficient for

superhydrophobicity but low hysteresis of the contact angle and the low sliding angle are the defining properties along with hydrophobicity for the formation of superhydrophobic materials.<sup>29</sup> For this reason reporting a static contact angle as the true angle of measurement is incorrect as this measurement will lie somewhere between the advancing and receding contact angles and can be as large as  $\pm 20^\circ$ . Contact angle hysteresis is therefore measured to determine the chemical and topographical homogeneity of the material being measured. There are two accepted methods for determining contact angle hysteresis and these will be discussed later.

### 1.2.3 Pinning of Water and the Red Rose

Water droplets can also be super-hydrophobic without the self-cleaning effect of the water droplet rolling on the surface. Different from the lotus effect, the so-called petal effect describes the phenomenon that a water droplet on the petal surface of a red rose (*rosea Rehd*) beads up, but does not roll off even when the petal is turned upside down.<sup>30</sup> This is known as “pinning” of the water droplet and can be described by the Wenzel wetting regime as depicted in Figure 1.3 a) above. The water penetrates into the structure of the surface and due to capillary force the water is “pinned” to the surface even through  $180^\circ$  rotation. This can also be seen commonly with the “sticking” of raindrops to the surface of glass windows. Inherent defects on the glass cause a rough surface and therefore pinning of the drop to the window. This drop will stay pinned until it becomes large enough through the incorporation of further drops (Oswald ripening) for gravitational forces to surpass that of the capillary forces acting on the drop and the drop is released from the surface. This normally occurs when the droplet reaches a critical size of 1mm in

contact with the surface.<sup>29</sup> The opposite of this can be seen in the Cassie wetting regime with a dual scale roughness. It can be seen that almost 95% of the surface of the rough material now in contact with the drop is air due to the energetically favoured bridging of the asperities, the air fraction of the material is defect free and allows unrestricted movement of the drop creating superhydrophobicity.

#### 1.2.4 Superhydrophobicity and the Lotus Leaf

Lotus leaves are a typical example of superhydrophobic natural materials that possess desirable self-cleaning and nonwetting properties with a water contact angle (CA) larger than  $150^\circ$  and a sliding angle below  $5^\circ$ . The lotus effect was first described by Barthlott,<sup>31, 32</sup> a botanist, with his study of the lotus leaf surface. It was found that the surface consists of numerous micropapillae with branchlike nanostructures, which is the very origin of the so-called lotus effect or self-cleaning effect. From Figure 1.7 a) these can be seen as microscale bumps on the surface of the leaf with nanoscale hair-like features covering the structure of the leaf. It has been suggested that this structure is preferential for the non-wetting of materials with the large papillae responsible for structural rigidity while the nanostructures reduce the surface area in contact with the liquid.<sup>24</sup>

The Cassie-Baxter wetting regime as described above is most commonly known due to the wetting seen on the lotus leaf and forms the basis of much recent scientific research<sup>33-37</sup>. This is not specific to the lotus and can be seen on other plants such as the rice leaf and silver ragwort<sup>38</sup>. Although all are superhydrophobic and botanic in nature a distinct variation in structure to achieve such hydrophobicity can be seen in Figure 1.7 a, and b displaying the variations in structure possible to



achieve such superhydrophobicity. This phenomenon allows for the rainwater hitting off the surface of the plant to remove dirt or dust particles away as the water rolls off the surface with only a few degrees of tilt as shown in Figure 1.8.

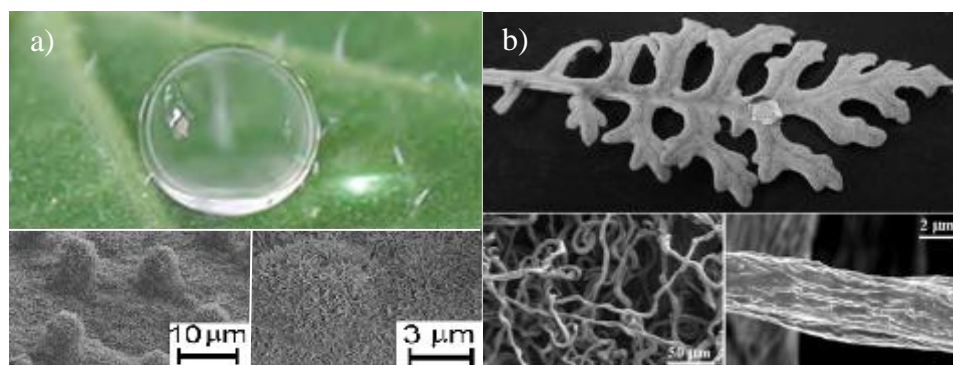


**Figure 1.7** a) The Lotus Effect with a spherical drop of water seen sitting on the surface of a lotus leaf with insert of high magnification SEM<sup>39</sup> and b) a similar effect seen on the silver ragworth with magnified SEM images of the surface structure.<sup>38</sup>

As discussed previously, the dual scale roughness is critical to the superhydrophobic characteristics of the leaf with Cheng et al.,<sup>39</sup> showing that the removal of the dual scale roughness on the surface of a lotus leaf through the annealing of the nanoscale hair like structure significantly reduced the contact angle of the leaf from superhydrophobic ( $\sim 150^\circ$ ) to a hydrophobic Wenzel like material with a contact angle of  $\sim 126^\circ$  seen. For the comparison of the removal of the papillae, a smooth carnauba wax was also analysed as a representative of the wax material seen on the surface of the lotus leaf. The carnauba wax displayed a water contact angle of  $\sim 76^\circ$ . It can be seen from the wax that the surface of the plant is not intrinsically hydrophobic due to the many hydrophilic functional groups (-OH, -COOH, -CHO) as shown by Herminghaus.<sup>40</sup> It can thus be deduced that it is the structure of the material that has greater effect on the wetting as compared to the chemical composition although also important. The microscale papillae were seen to

be responsible for the increase in contact angle from  $76^\circ$  to  $126^\circ$  and the nanoscale, hair like structure responsible for the further increase in contact angle up to  $150^\circ$  with surface chemistry having a greater effect on the ability of water to wet the surface through mechanical means rather than static contact angle formation.

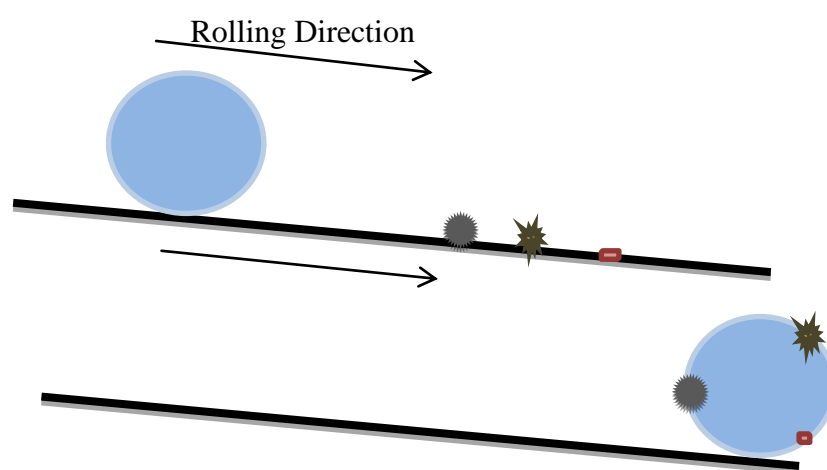


**Figure 1.8** Schematic representation of the self-cleaning effect as seen on the lotus leaf.

A further study into 33 different variations of superhydrophobic plants by Wagner et al.,<sup>41</sup> showed that the shape, size and aspect ratio of the surface roughness also effects wetting. It was shown that micropapillae were seen to give the greatest contact angle as compared to convex shape structures with a finite aspect ratio (height/distance of papillae) of  $<1$  seen to give the greatest hydrophobicity. Due to the size and structure of the surface the creation of a fragile air-layer trapped in the spaces between the microstructures could be formed. Increasing the distance between the microstructure increased the water/air contact area thus increasing contact angle. However, the water drop may penetrate more easily into the spaces by its own weight or high impact velocity and wets the surface. It was seen that equilibrium must be met between the height of the microstructures and the distance

between them. Larger microstructures gave less stable surface wetting with reduced contact angle, whereas a larger amount of smaller microstructures seemed more effective in terms of water repellency.

Other interesting examples of hydrophobicity in nature include the Pygmy Gecko (Figure 1.9 a), which due to being as small as the top of your finger has the possibility of drowning in a droplet of water. Due to this, it has developed hydrophobic skin which enables it to stand on the surface of water and has been dubbed “unsinkable”. The fishing spider b) with roughened legs enables it to glide across the water’s surface, and the Basilisk Lizard c) which has been dubbed “the Jesus Christ Lizard” due to its ability to “walk on water”.



**Figure 1.9** Examples of the use of hydrophobicity in nature with a) the Pygmy Gecko, b) the Fishing Spider, and c) the Basilisk Lizard.

From the studying of the structure of the lotus and other such plants, synthetic surfaces with unique properties of superhydrophobicity can be potentially used as self-cleaning glass, car windshields, solar cells, marine vessels and aircrafts, and in low-friction pipelines<sup>42</sup>. Moreover, these superhydrophobic surfaces can be used in the prevention of fogging, icing, snow sticking, and oxidation.

### 1.3 Applications

Most applications of hydrophobic materials are focused on superhydrophobic self-cleaning coatings. Such coatings have a self-cleaning, anti-corrosion effect on surfaces leading to widespread application through many diverse sectors. The most commercially successful route to hydrophobicity so far has been to modify existing paint technology<sup>43</sup>. Paints typically contain particles, solvent, and a polymeric binder. If the particle loading is high and binder content is low, as the solvent evaporates, particles or aggregates distort the binder to generate a roughened surface. This is the most common method used in commercial products. Methods like this can generate very effective hydrophobic surfaces with mostly random texture.

The BCC market research report ‘Nanotechnology in coatings and adhesive applications’ shows a current market for nanocoatings of €3 billion in 2010 expanding to €15 billion by 2015. Superhydrophobic coatings are a key category of nanocoatings used for self-cleaning applications in construction, textiles, military and electronics and are worth 10% of this entire sector currently 0.3 billion expanding to 1.6 billion by 2015 ( Table 1.2).<sup>42</sup>

**Table 1.2:** Areas of commercial application of superhydrophobic coatings and projected market

	2010 (€million)	2015 (€million)
Construction (Self Clean)	26.2	113.7
Construction (Anti-microbial)	34.8	114.2
Health (Anti-microbial self-clean)	49.5	288.9
Military (Self Clean)	17.5	102.6
Military (Anti-ice)	17.6	96.8
Fabric (Stain Repellent)	96.6	423.5
Electronics (water moisture repellent)	11.7	74.6
Transport (Self Clean)	128.0	417.7

There are several companies active in the areas of nanocoatings specialising in superhydrophobic coatings. One of the earliest and most widely recognised commercial trade names is that of Gore-Tex® which is a superhydrophobic polytetrafluoroethylene (PTFE) material patented in 1972 and a market leader in waterproof materials with worldwide sales of \$3 billion in 2011.

One large scale use of nanomaterials in the commercial sector has been seen with a forerunner in the airline industry. EasyJet airlines have recently undertaken a project to increase the fuel efficiency of their fleet with the application of a nanomaterial based coatings. The coating which has previously only been seen for military use is now being used in the commercial airline industry. This application in the commercial sector illustrates the reduction in costs of applying nano-based coatings as manufacturing and production costs are reduced to make them commercially viable. EasyJet is the first U.K airline to coat their fleet with nanotechnology developed coatings to replicate a macroscopically smooth surface by filling the voids on the planes surface, reducing drag in flight and thus reducing fuel consumption costs. The coating is applied through an electrostatic coating process. The use of such coatings can be seen to be easily viable in the current economic climate with increasing costs in aviation grade fuel with an increase in price of 2% since 2011, with EasyJet alone spending £750million on aviation grade fuel in 2011. The increase in fuel costs may see the development and greater use of such coatings in the future with EasyJet stating on their company webpage that “an easyJet passenger is responsible for 22% fewer emissions than a passenger on a traditional airline, when they fly the same route and use the same type of plane”<sup>42, 44</sup>. As a comparison to the relatively high cost aviation sector, the construction industry is seen as a user of large scale and low cost materials. The use of nanomaterial’s within

the construction sector however is seen to rise due to high value properties associated such new material's at relatively low additive costs. The self-cleaning and anti-fogging properties of window glass is seen as one area of increased interest in this sector due to large costs seen in the commercial cleaning of windows on high-rise buildings. Specialised anti-reflective coatings can also be seen in nanocoatings of this type with dual scale roughness shown to reduce the reflectance of light on the external side of a window allowing more light through and increasing reflectance on the internal side of the window decreasing the U-value of the window with reductions of 4% in heating costs with an increase in natural light<sup>45</sup>. The reflectance of different textured samples can be seen in Table 1.3.

**Table 1.3** *Weighted Reflectance on different Textured Surfaces*

<b>Sample</b>	<b>Weighted Reflective %</b>
<b>Flat Si surface</b>	37.3
<b>Pyramid-textured surface</b>	12.3
<b>Nanotextured surface</b>	6.4
<b>Two-scale textured surface</b>	3.8

One use of anti-reflective coatings can be seen here to increase the amount of light entering a building while also reducing the amount of heat escaping, reducing costs in an environmentally friendly low impact way. Incorporation of, or coating with  $\text{SiO}_2$  and  $\text{TiO}_2$  nanoparticles within these layers also allows “added value” functions for window glass, pavement, walls, and roofs. Silica nanoparticles incorporated between two glass panels can fireproof windows,<sup>43</sup> further increasing the value of the incorporated nanocoating.

The use of antireflective coating (ARC) through the use of dual scale superhydrophobic coating also has potential applications in the photovoltaic (PV) industry. Renewable solar energy relies on the harvesting of energy from photons of light with sufficient energy to penetrate the semiconductor material and excite electrons into the conduction band for the production of electricity. The efficiency of the PV device to convert light energy to electricity is essential. With the use of an ARC on the surface of a PV, the reduction of reflected light and thus the increase in transmittance results in increased efficiency of the solar panel. The use of an ARC can thus be transferable from device to device with increased efficiency through the application of a thin coating rather than altering the device fabrication or the chemistry of the material. The current industrial method for the fabrication of ARC on PV devices is the use of plasma enhanced chemical vapour deposition (PECVD) of silicon nitride (SiN). This method however is an expensive route towards ARC's<sup>46</sup>. The use of colloidal particles<sup>47</sup> have shown to be an efficient ARC with the use of silica (SiO<sub>2</sub>) nanoparticles. These SiO<sub>2</sub> nanoparticles have shown to reduce reflectivity by approximately 12% which leads to an increased efficiency of roughly 5% through a relatively inexpensive colloidal approach. Theoretically, the reduction in the reflectance of light can be demonstrated through the Fresnel equation, (Equation 4) where it is shown that a minimum reflectance of light can be created through the control of the thickness of the coating and the refractive index of the coating used as compared to the substrate.

$$R_m = \left( \frac{n_c^2 - n_1 n_2}{n_c^2 + n_1 n_2} \right)^2 \quad \text{Eq. 4}$$

where  $n_c$ ,  $n_1$ , and  $n_2$  are the refractive indices of coating, medium, and substrate, respectively. In order to reduce reflectance towards zero, the refractive index of the coating must satisfy the condition

$$n_c = (n_1 n_2)^{1/2} \quad \text{Eq. 5}$$

with the thickness of the coating determined by the equation:

$$t_c = \lambda_0 / (4n_c) \quad \text{Eq. 6}$$

Where  $\lambda_0$  is the wavelength of light where zero reflectance is required. From these calculations it can thus be determined that the desired properties of an ARC on a silicon substrate in an air environment must have a refractive index of 2 and have a layer thickness of 75nm<sup>48</sup>. Thus through the use of a colloidal approach for the fabrication of nanoparticles and the control of the refractive index of the material an ARC can be manufactured.

Due to the broad range of potential applications for such coatings the nanomaterial market is currently a business sector which has seen large growth with rapid expansion and ever increasing interest from various markets. Currently however there is no brand leader with a strong share of the market due to most current coatings, although fit for purpose, not capable of multifunctionality due to inherent flaws within the material either in production methods or end properties of the coating. Below are some examples of currently available superhydrophobic coatings:

1. *Cleancorp nanocoatings, Birmingham UK* use 10 nm ceramic particles as superhydrophobic coatings for metal, ceramics and stone and are active mainly in the construction sector. The advantage of ceramic nanoparticles is



that they can be formed in high volume relatively cheaply with the disadvantage that the contact angle is insufficient for a complete self-cleaning effect.

2. *Cotec GMBH, Karlsten Germany* use plasma and CVD processes to generate nanostructured surfaces for self-cleaning coatings in electronics. The advantage of this process is that the contact angle is engineered for exact surface construction. The disadvantage is CVD processes are expensive, not scalable and only suitable for niche applications
3. *DFI San-Clemente, California* use Silicone technology as self-cleaning coatings for health applications. The advantage of this technology is that the coating is chemically processable, with the disadvantage of the reliance on polymer based coatings which are not suitable for exterior applications and delaminate from surfaces readily.

The implicit challenge identified in these examples is that a lot of the technologies which can achieve high contact angles require expensive materials or do not survive the demanding environment of outdoor testing, whereas less expensive methods do not form the necessary contact angle. Although certain limitations are being experienced currently in the field of nanocoatings, the broad ranging applications and demand for such coatings will inevitably lead to the production of superior coatings.

## 1.4 Methods for the Preparation of Superhydrophobic Surfaces

The lotus effect and thus its potential applications have inspired numerous attempts to fabricate superhydrophobic surfaces on a variety of different surfaces including polymers<sup>49</sup>, semiconductors<sup>30</sup>, and metallic surfaces<sup>50</sup>. The surface roughness of the lotus has been emulated using structures such as nanopillars<sup>51</sup>, nanofibers<sup>52</sup>, to nanospheres<sup>53</sup>, by the introduction of porosity into materials<sup>54</sup> or by top-down methods such as lithography<sup>55</sup> to bottom-up approaches such as self-assembled monolayers (SAM) of low surface energy materials<sup>56</sup>. Initial work through polymers showed that the largest contact angle through use of polymer chemistry achieved initial contact angles up to 110°. Nishino et al.<sup>6</sup> measured the surface of regular aligned closest hexagonal packed  $-\text{CF}_3$  groups. *n*-Perfluoroeicosane was vapor deposited onto glass and gave epitaxially grown single-like crystals with a contact angle with water of 119° seen, which corresponded to a surface free energy of 6.7 mJ/m<sup>2</sup>. This value is considered to be the lowest surface free energy of any solid, based on the hexagonal closed alignment of  $-\text{CF}_3$  groups on the surface.

### 1.4.1 Polymer Materials

The use of polymer materials seems a logical one for use as a hydrophobic material due to their inherently low surface energy. Polymer materials form one of the largest areas of research towards fulfilling the ideal superhydrophobic self-cleaning material. Several different approaches are taken to achieve the greatest contact angle while maintaining physical durability of the material produced.

Polydimethylsiloxane (PDMS) belongs to a group of organosilicon compounds and is a common precursor in the production of superhydrophobic polymer based materials. The intrinsic deformability and hydrophobicity of PDMS makes it a suitable material for producing hierarchical scale superhydrophobic surfaces. Various methods are practised to produce superhydrophobic surfaces using PDMS, such as that used by Khorasani *et al.*<sup>57</sup> through surface modification of PDMS using a CO<sub>2</sub> pulsed laser as an excitation source to introduce peroxide groups onto the PDMS surface. These peroxides are capable of initiating graft polymerization of 2-hydroxyethyl methacrylate (HEMA) onto the PDMS. The water contact angle of the treated PDMS was measured to be 175°, and shown to be somewhat stable over prolonged water contact angle measurements. The reason for such an increase in water contact angle is due to porosity and chain ordering on the surface of the PDMS. Jin *et al.*<sup>58</sup> used a PDMS elastomer containing micro and nanocomposite structures to produce superhydrophobic surfaces. They employed a laser cutting method to induce roughness on the PDMS surface. The surface produced by this technique exhibited water contact angle as high as 160° and sliding angle as low as 5°.

With roughness having a quantitative effect on the contact angle with polymer materials, as all materials, a great deal of effort is being placed on controlling the size and shape of these features. Due to the ability of polymer materials to deform, nanopatterning of asperities on polymer surfaces has become a large area of scientific interest with the control of the size of asperities,<sup>59</sup> and aspect ratio<sup>60</sup> showing the ability to manipulate the microscopic contact angle through the alteration of the nanometric surface topography.

### 1.4.2 Electrospinning

Electrospinning is a method whereby the formation of polymer based fibres can be produced into a continuous layer. The method employs electrostatic forces to stretch a polymer jet for the production of superfine fibres. With the use of hydrophobic starting materials, superhydrophobic mats with sufficient roughness can be produced and have been demonstrated with the use of polymers,<sup>61</sup> block copolymers,<sup>62</sup> inorganic<sup>63</sup> and hybrid (organic/inorganic)<sup>64</sup> materials. Lim et al<sup>52</sup> showed that through the incorporation of colloids to the fibrous structure produced, as seen in Figure 1.7 a), water contact angle of the electrospun mat could be increased. The increase in water contact angle was attributed to the increase in roughness through the incorporation of colloids.

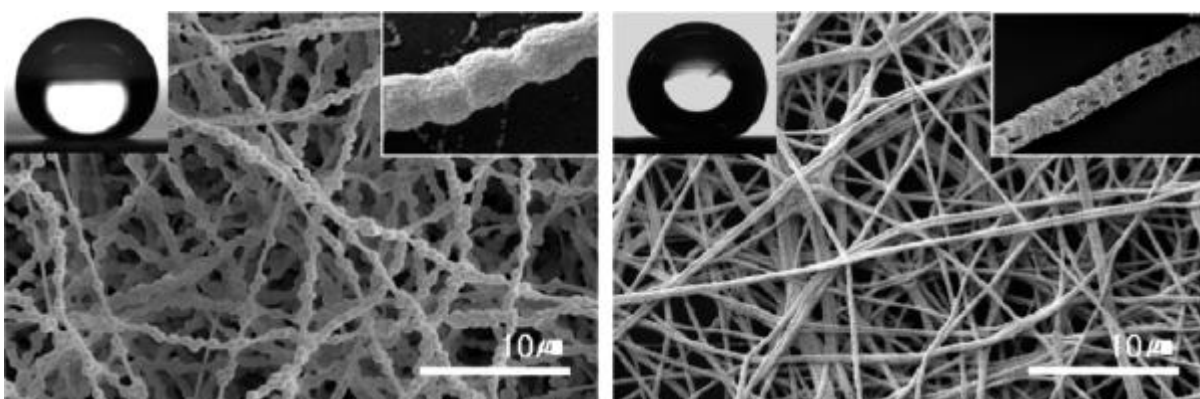


**Figure 1.7** SEM images of electrospun composite nanofibers with silica particles a) and without b) with inserts of water contact angle and high magnification SEM.<sup>52</sup>

### 1.4.3 Chemical Vapor Deposition (CVD)

Chemical vapour deposition (CVD) involves the formation of crystalline inorganic thin films produced from a gaseous precursor. CVD enables the formation of single structures due to the growth of self-assembled crystallites on a suitable

substrate. Due to this growth mechanism CVD generally promotes the growth of nanorod and nanowire like structures

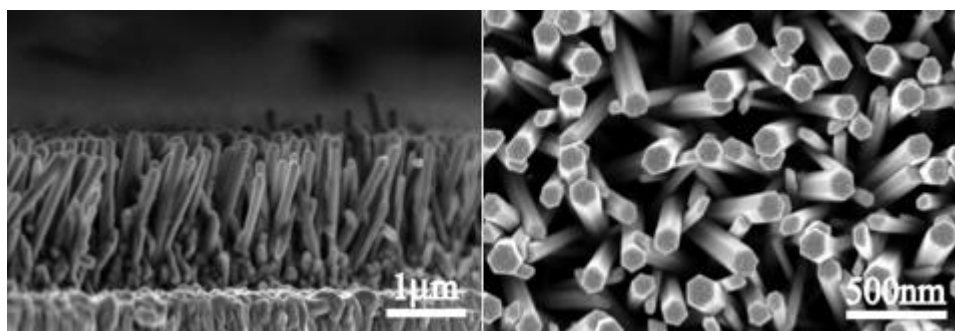


**Figure 1.8** *Controlled growth of vertically aligned nanorods through CVD.*

Use of CVD for the creation of hydrophobic materials can be seen in the work of Feng et al., (Figure 1.8)<sup>51</sup> with the controlled growth of vertically aligned nanorods. Use of CVD can also be seen in the coating of a roughened surface with a low surface energy material such as teflon<sup>65</sup> or octadecyltrimethoxysilane.<sup>66</sup> Carrying on from this work, Hosono et al.<sup>25</sup> fabricated metal hydroxide nanoneedles through a chemical bath deposition (CBD) method. The use of a needle shape dramatically reduced the solid fraction in contact with water, (as displayed in the legs of the water strider) and thus increased hydrophobicity according to Young's equation (Equation 2). This allowed for the formation of superhydrophobic materials with the use of high surface energy materials such as metal oxides and hydroxides with one of the largest contact angles of 178° seen to date.

Another area of growing interest not only for their vast chemical, electrochemical and mechanical properties is the use of carbon nanotubes (CNT) as a superhydrophobic material. CNT's can be grown through CVD methods and allow for vertical alignment of carbon nanotubes which are similar in structure to that of

porous materials. CNT's have shown contact angles of  $160^{\circ}$ <sup>67</sup> and have added value to superhydrophobic materials due to their increased tensile strength.

#### **1.4.4 Etching and Lithography**

Lithography is a method used for the fabrication of rough surfaces with regular structures due to the control of surface structure size. For example, Öner and McCarthy<sup>68</sup> have employed photolithography to transfer the patterns of masks onto silicon wafers and increased the contact angle through the silanization of the patterned surface. This has allowed the controlled fabrication of nanopillars of different length scales, and has shown that contact angle can be independent of post height from 20 - 140 $\mu$ m for several different surface modifications. Surface shape has also been an area of scientific interest with much work done on how shape affects the wetting behaviour of materials. Del Campo et al.<sup>69</sup> have shown that varying the contact shape variation in adhesion of the liquid is greatly affected. It was seen that mushroom like pillars can increase adhesion of the drop by up to thirty times as compared to a flat pillar surface. The use of hierarchical surface roughness can also be determined with ideal dimensions.

Besides the above physical methods, chemical etching is employed for surface roughening on polycrystalline metals, such as aluminium, copper, and zinc<sup>70</sup>. Compared with physical methods, chemical etching is a simple technique, but generates irregular surface structures. In general, lithographic methods are too complicated to form large scale superhydrophobic surfaces.

### 1.4.5 Physical Vapour Deposition (PVD)

The most common and oldest form of metal evaporation is thermal evaporation, and is one of the simplest vacuum deposition methods. Thermal metal evaporation is widely used in industry to produce metal films for applications in food packaging and labelling. Metal evaporation at an industrial scale is high rate, roll-to-roll coating with line speeds exceeding 1,000m/min.<sup>71</sup>

Thermal evaporation involves the heating of a metal sample holder which contains the solid metal sample to be deposited. The sample boat normally contains a dimple to hold the solid sample and is heated through a high current which is passed through the resistive sample holder. This causes the metallic sample to melt and wet the sample holder. As the temperature increases the metal evaporates. Most evaporations are done under high vacuum, ( $\sim 10^{-6}$  Torr), and cause the metallic evaporated particles to travel towards a sample holder placed above the evaporation boat. The metal condensates as it hits the sample and coats the material with the metal being evaporated. The metal will then rapidly cool forming a solid metal coating on the sample. Metal coatings of controlled thickness down to the nanometre scale can be controllably evaporated.

From the evaporation of metals various film formations can occur. Film formation has classically been divided into three separate growth modes depending on how the metal interacts with the substrate upon contact, with each displaying physical characteristics upon formation. If the affinity of the substrate for the deposited particle is strong, a two-dimensional growth mode will occur until complete coverage of the substrate. Subsequent layers will then grow layer-by-layer. This growth mode is known as Frank-Van der Merwe<sup>72</sup> mode and is common in the

epitaxial growth of semiconductor films as seen in Figure 1.9 a). The opposite will also occur if the affinity of the deposited particles towards each other is high or towards the substrate is low. This growth mode is known as Volmer-Webber (VW)<sup>72</sup> growth and is evident with metals grown on oxides occurring in this fashion. This growth mode results in the formation of metallic “islands” on the surface of the substrate and can be easily determined with the use of a scanning electron microscope (SEM) and can be seen in Figure 1.9 c). If neither affinity towards substrate nor deposited particle is high an intermediate mode is achieved with initial film growth and island formation occurring on top of the film with this film growth seen in Figure 1.9 b). This intermediate can also be seen when substrate-particle affinity is initially high, but a lattice mismatch between the film and the substrate introduces a strain into the growing film causing the creation of islands upon the film. This intermediate growth mode is known as Stranski-Krastinov<sup>72</sup> growth mode.

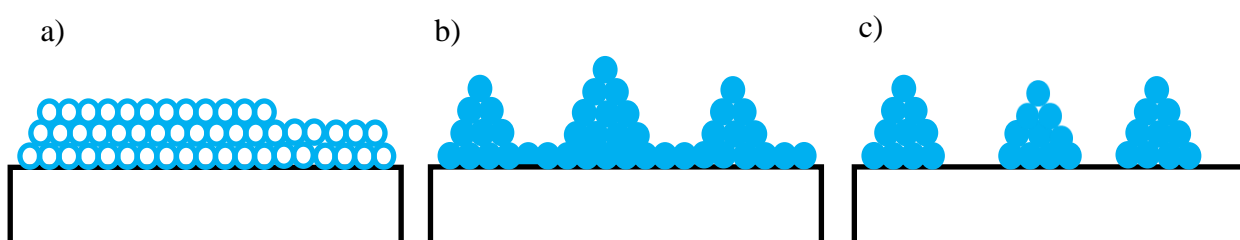


**Figure 1.9** Film growth modes a) layer-by-layer growth or Frank-Van der Merwe film formation b) Stranski-Krastinov growth and c) Volmer-Weber, or island growth formation.

The evaporation of metals is seen not only through thermal deposition but also through techniques such as laser ablation,<sup>73</sup> plasma arc deposition,<sup>74</sup> sputtering,<sup>75</sup> and chemical vapour deposition (CVD)<sup>76</sup> methods with each method capable of film formation through the various growth methods as described above. The use of metals in superhydrophobic materials is limited to methods employed to



impart hydrophobicity on intrinsically high surface free energy metals, rather than the use of metals to impart hydrophobicity through a roughening of the surface. This was seen by Qian and Shen<sup>70</sup> who through dislocation-selective chemical etching of Aluminium (Figure 1.10 a), Copper, and Zinc substrates created sufficient surface roughness to increase hydrophobicity which was further increased through the coating of the metallic surface with fluoroalkylsilane to increase hydrophobicity up to 156°.

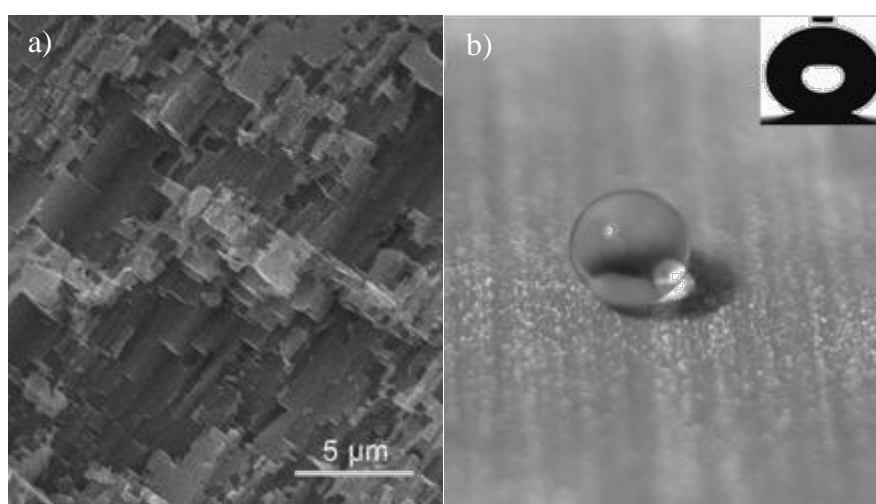


**Figure 1.10** a) SEM image of aluminium etched with a Beck's dislocation etchant and b) a water droplet displaying high contact angle on the fluoroalkylsilated surface.<sup>70</sup>

The use of high surface energy metals seems counterintuitive for the development of a superhydrophobic surface due to the fact that Young's equation, (Equation 1) states that low surface energy materials will increase the water contact angle of a liquid drop. The contradiction arises with the use of metals, which are intrinsically high surface energy materials in the preparation of superhydrophobic materials<sup>50, 77-79</sup> with high contact angle and low hysteresis. One example where metallic materials have been utilized in the formation of superhydrophobic coatings without modification through high surface energy materials has been demonstrated

by Bromashenko<sup>78</sup> et al. with the use of sputtered chromium on hot pressed crimped Poly(vinylidene fluoride) PVDF beads. Although the PVDF layer is a low surface energy material the liquid phase has no interaction with this surface due to the evaporation of a chromium layer as seen in Figure 1.11 with a contact angle of 150° demonstrated.

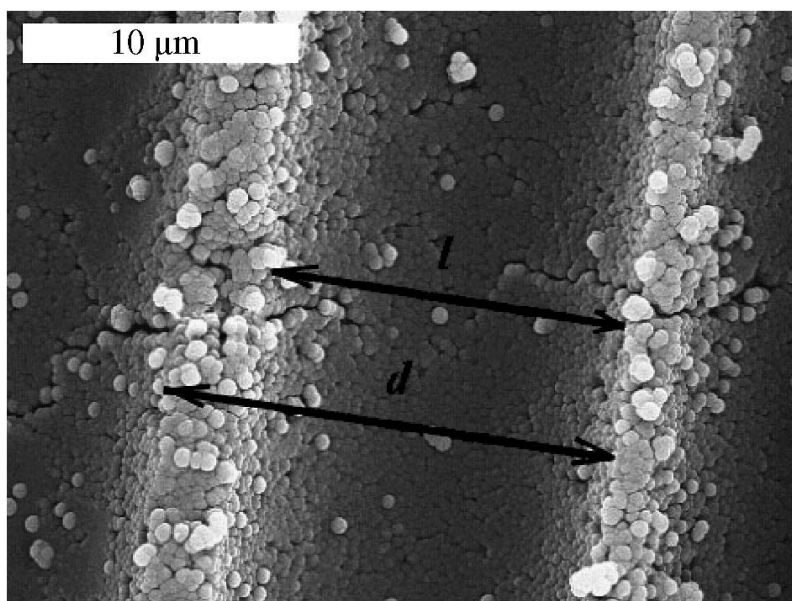


**Figure 1.11** SEM image of the fine structure of the polymer channels coated with chromium<sup>78</sup>

The use of evaporated metals allows for the incorporation of a double roughness, or hierarchical nanoscale roughness to the material, mimicking the surface topography of the lotus and other such superhydrophobic surfaces. This roughness as described by Wenzel<sup>7</sup> and Cassie-Baxter,<sup>8</sup> decreases the solid fraction in contact with the liquid. A stable solid/air composite is formed with up to only 5% of the solid material now in contact with the liquid with the remaining supported by air trapped between the crenels on the surfaces created by the Volmer-Weber evaporated metal growth. This large air fraction now in contact with the liquid drop as described by Cassie-Baxter which is intrinsically defect free and low in surface energy, allows the

use of high surface energy materials such as metals for use as superhydrophobic functional materials allowing the desirable mechanical properties of metals to be incorporated onto the surface of the substrate with added value for use as superhydrophobic surfaces. The use of metals through evaporation allows the particles to be strongly bound to the substrate as compared to ligand capped,<sup>80, 81</sup> fluorinated<sup>82, 83</sup> polymer equivalents which are UV-sensitive and degrade over time.

#### **1.4.6 Layer-by-Layer and colloidal Assembly**

Colloidal assembly is an attractive form of fabrication of nanoscale hydrophobic materials. Colloidal assembly allows for the formation of assemblies with nanoparticles of varying size with controlled size dispersion<sup>84</sup>. This small size dispersion facilitates the formation of close packed assemblies either through self-assembly or layer by layer assembly. This allows for the potential of cheap and large scale formation of superhydrophobic coatings. A popular method for the creation of colloidal assemblies is through the gravitational sedimentation of colloids in suspension. This area has seen a great deal of effort from theorists and experimentalists due to the potential use as photonic band gap materials with applications in the photonic and electronics sector<sup>85</sup>. The self-assembly method however has also shown to be successful in the preparation of highly ordered and well defined monolayers/multilayers for the formation of superhydrophobic coatings. The ability to create a surface coating of sufficient dimensions for practical applications with the use of micro- and nano-sized particles while maintaining the inherent properties of those particles, such as hydrophobicity, is one main advantage of the technique. A colloidal assembly of SiO<sub>2</sub> spheres is shown in Figure 1.12 demonstrating the close packed hexagonal structure created from colloidal assembly.

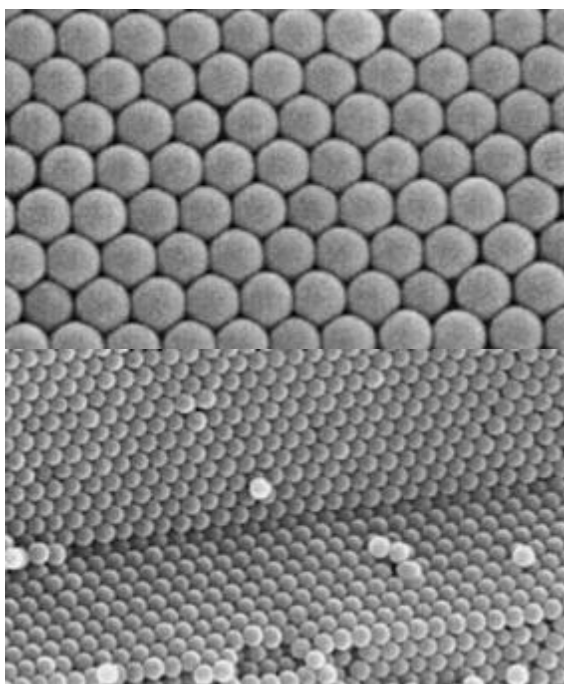
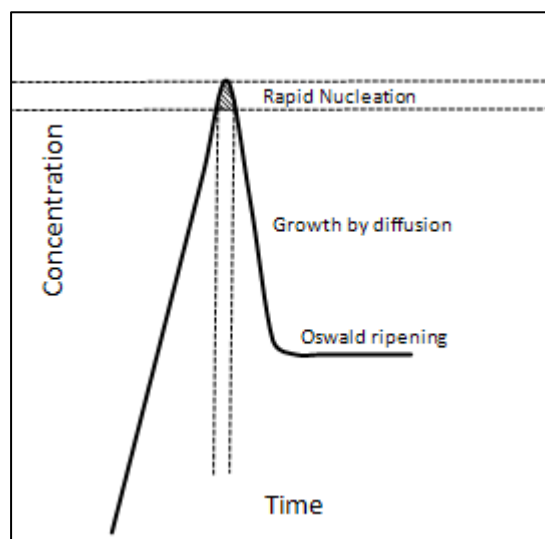


Figure 1.12 SEM images of self-assembled SiO<sub>2</sub> particles and thermally annealed at 950°C<sup>85</sup>.

The use of colloidal assemblies has shown to be effective in the formation of superhydrophobic coatings with the use of three-dimensional (3D) polyvinylidene fluoride (PVDF) macroporous films by Li et al.<sup>54</sup>. It has been shown that the roughness induced through the creation of such colloidal assemblies increases the water contact of the materials<sup>86, 87</sup> as described by Wenzel. Colloidal assemblies therefore allow for the creation of a relatively rough, homogenous coating which can impart the hydrophobic nature of the building block material across a relatively large and repeatable surface area. This surface is facilitated through the creation of homogenous particles of a controlled size and shape through the specific tailoring of particle growth conditions<sup>84</sup>.

### 1.4.7 Growth of particles

In general for the formation of all nano and sub-micron particles to grow in a monodisperse fashion, the initial nucleation and growth of the particles must occur in controlled separate stages. It was first suggested by Le Mer<sup>88</sup> that if the concentration increases rapidly, rising above the saturation concentration a rapid burst of nucleation can occur within the solution with the formation of a large number of nuclei. The formation of nuclei will thus reduce the concentration below the saturation concentration where particle growth can occur. This nucleation and growth model is displayed below in Figure 1.13. The Le Mer model supplies a key idea that both the nucleation and growth phases when separated give almost monodisperse particles.



**Figure 1.13** Ideal Nucleation and growth phases as per the Le Mer particle growth mechanism.

It suggests that if the nucleation phase occurs in several stages or over a longer period of time, particles will have separate growth histories resulting in differing particles sizes. Continuing on from the work of LaMer with the study of particle nucleation and growth, certain parameters have been identified in the control of

particle size. If the formation of particles occurs as described with a separate single rapid nucleation phase followed by a continual growth phase average particle size can be determined by the relationship between the initial number of monomers present and the final number of particles.

$$\text{Average Particle Size } (S) = \frac{T \text{ (number of monomers)}}{N \text{ (Final particle number)}} \quad (\text{eq. 5})$$

From this relationship it can be seen that due to the fixed number of monomers available, an increased final number of particles will result in a reduced average particle size. To facilitate the separation of nucleation and growth phases in the formation of colloidal particles a two stage reaction mechanism is normally incorporated such as that in the Stöber synthesis for silica colloidal particles. Formation generally occurs with the reaction taking place via hydrolysis of the silyl ether to a silanol (nucleation) followed by a condensation reaction (growth) with the formation of particles in the range of ~50nm - ~2µm<sup>89, 90</sup>.

An area where the production of superhydrophobic colloidal materials has not received much attention is through the use of supercritical-CO<sub>2</sub> for the formation of colloidal superhydrophobic particles of controlled size for the production of colloidal assemblies.

## 1.5 Supercritical Carbon Dioxide

Supercritical carbon dioxide (sc-CO<sub>2</sub>) refers to carbon dioxide that is in a semi-fluid state when elevated above its supercritical temperature (31.1°C) and pressure (73.7 bar / 1070.4 psi)<sup>91</sup>. This can be seen in the phase diagram of carbon dioxide below (Figure 1.14). Supercritical fluids have novel properties. The supercritical phase has a lower viscosity of the liquid phase with high diffusivity similar to the gaseous phase. This allows for rapid mass and heat transfer. Supercritical fluids have a characteristic diffusivity of 10<sup>-3</sup> cm/s as compared to that of a gas of 10<sup>-1</sup> cm/s and 10<sup>-5</sup> cm/s for that of a liquid. These unique properties allow supercritical fluids the solvent power of a liquid while maintaining the diffusivity of a gas<sup>92</sup>. This facilitates the use of carbon dioxide as a carbon neutral green solvent capable of replacing the common organic solvents which can be potentially harmful and difficult to dispose of.

The point at which a gas or a liquid becomes a supercritical fluid can be described with the use of phase diagrams. A phase diagram provides a visual understanding of the unique characteristics of supercritical fluids. The point at which the transfer into a supercritical fluid occurs is known as the critical point. Along the line from the triple point to the critical point, the density of the gas increases while the density of the liquid decreases until the critical point is reached where the two densities become equal to each other, leading to one phase termed as supercritical fluid. It is within this region where temperature and pressure can be increased with the supercritical phase remaining constant. Supercritical-CO<sub>2</sub> is becoming an important commercial and industrial solvent due to its role in chemical extraction in addition to its low toxicity and environmental impact.

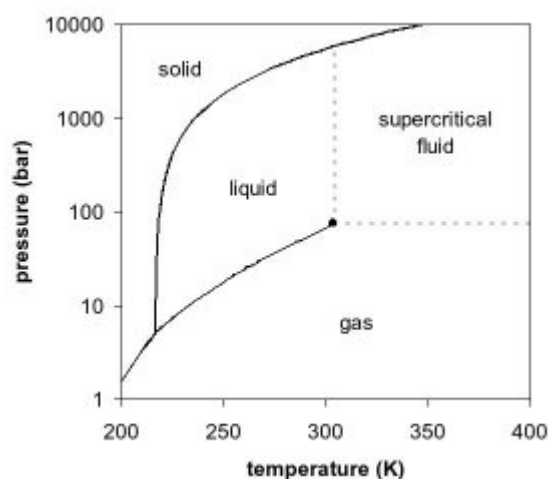


**Figure 1.14** Phase diagram of carbon dioxide.

The ability to use sc-CO<sub>2</sub> as a solvent will depend on the polarity of the solution and its interaction. Sc-CO<sub>2</sub> has a relatively low critical point allowing most compounds to be stable in these conditions. Carbon dioxide (O=C=O) is a nonpolar molecule with some polarity due to its quadrupole moment. Solubility is a defining feature of how best to utilize supercritical carbon dioxide for a specific application. Small non-polar or slightly polar compounds are fully miscible with sc-CO<sub>2</sub>. Heavy and/or polar molecules are poorly soluble in supercritical carbon dioxide, but the solubility of such compounds can be enhanced by adding a small amount of co-solvent, such as acetone, methanol or ethanol<sup>92</sup>.

The formation of particles from sc-CO<sub>2</sub> is a common use of supercritical fluids due to its low cost and benign working conditions. Several techniques are currently available for the production of particles with the use of supercritical carbon dioxide as a solvent. The process of rapid expansion from a supercritical solution (RESS) can be used where the material is highly soluble in the supercritical medium. This process is therefore mainly used on organic materials due their large solubility



in supercritical carbon dioxide. The process involves the expansion of a supercritical solution into a reduced pressure vessel through a specially designed orifice to achieve the desired particle size. The important parameters to consider in the formation of particles from RESS is that not many materials are highly soluble in sc- $\text{CO}_2$  and that the orifice used must be capable of supporting a large pressure drop without freezing. This can be supported through the use of a throttling valve, capillary tube or needle valve. RESS has been demonstrated in the formation of particles,<sup>93</sup> thin films,<sup>94</sup> and fibres.<sup>95</sup> The supercritical fluid can also be used as an antisolvent in the formation of nanomaterials. The Gas antisolvent (GAS) technique<sup>96</sup> uses the supercritical fluid to act as an antisolvent and participate a solute from an organic solvent. With the ability of the SCF to diffuse into the soluble liquid phase of the organic solvent the non-soluble phase is forced to precipitate from solution with the formation of particles. Particle formation can be controlled through gas expansion rate and concentration of the solute in the initial organic solvent.

## 2 Characterisation Techniques

Characterisation of the particles produced was important for understanding how the particle and subsequent films formation affected the water contact angle. Due to the small nature of the particles produced, electron microscopy was an important instrument for visualisation of particles and films. The use of scanning electron microscopy (SEM) allowed for analysis at the sub-micron scale and allowed for the characterisation of changes at this scale and their effect on the macroscale properties of the material.

### 2.1 Scanning Electron Microscope

The scanning electron microscope (SEM) that was used in the analysis and characterisation of materials were obtained with a Hitachi SU-70 system operated from 3 to 20kV. Scanning electron microscopes allow for increased magnification of objects up to 300,000x magnification as compared to a few thousand times magnification seen on an optical microscope. SEM's have a large depth of field allowing for a three dimensional representation of the object being imaged. The setup of the instrument allows for the high magnification and large depth of field seen with SEM. Figure 2.0 depicts a standard SEM setup.

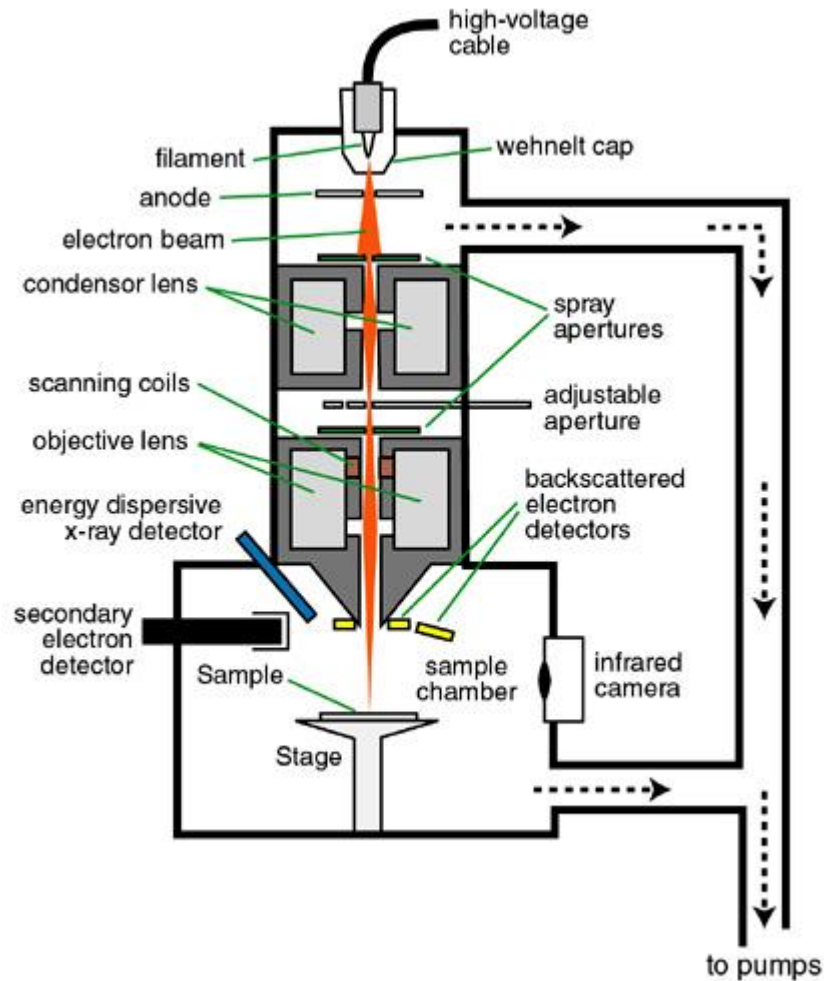


**Figure 2.1** Scanning electron microscope overview.

The source of electrons is created from at a high voltage filament. The electrons created at the source are attracted towards the anode and condensed towards a sample stage. The SEM contains a small electron probe 1-10nm in diameter and scans in a raster across the surface of the sample where electron interaction with the sample creates electron scattering. The rastering or scanning of the focused beam over the sample is what gives SEM its name. The scattered electrons are then collected through a detector, passed through a photomultiplier (PM) tube and displayed as an image. Filament selection can play an important role in maximum resolution available with several options available. A tungsten filament

is the most basic filament available. This filament is cheap however is not as bright, ( $1 \times 10^4$  A/cm<sup>2</sup>sr.kV) or have as long a life span (200 hours) as compared to a Schottky filament source which is brighter ( $1 \times 10^7$  A/cm<sup>2</sup>sr.kV) and has a lifespan of over >2000 hours. Resolution of the tungsten filament source is also reduced due to a source size with resolution of 10nm seen at 3kV as compared to the Schottky field emission filament source which allows a resolution of 1.6nm at 1kV. Other sources of filaments include cold and thermal field emission (CFE & TFE) sources which have comparable brightness and life span to the Schottky filament with reduced source size to below 5nm thus increasing the resolution potential of the instrument. These filament sources however are not as stable as the others with Cold Field Emission needing cathode regeneration every 6 to 8 hours. The filament of choice for general SEM use is the Lanthanum Hexaboride (LaB<sub>6</sub>) cathode which has average brightness ( $1 \times 10^5$  A/cm<sup>2</sup>sr.kV) and source size (5 to 50µm) allowing resolution of 2nm at 30kV. The source used in this analysis work was a Schottky field emission source allowing for greater resolution at lower accelerating voltages.

As the electron beam produced from the filament is focused through a pair of electromagnetic optical and condenser lenses. The path of the electron beam can be altered by exposure to this magnetic field. Electromagnetic lenses create a circular magnetic field that condenses the electron beam as it passes through. The strength of the lenses can be changed by varying the current supplied to the lens. Changing the lens current changes the focal length of the lens and thus bringing the sample into focus depending on the sample distance from the probe. As the beam hits the sample the electrons interact with the sample through elastic or inelastic scattering. Elastic scattering results in the production of backscattered electrons where the primary electron comes close to the nucleus and alters the path of the primary electron with a

minimal loss in electron velocity. If such an electron leaves the sample specimen it is known as a backscattered electron. The number of backscattered electrons emitted from a specimen is dependent upon the atomic number of the specimen and thus can be used for elemental contrast.

Inelastic scattering results in the production of secondary electrons which are formed due to the penetrating electrons colliding with the nucleus or an electron of an atom of the specimen. The primary electron undergoes a change in direction, as well as transferring energy to the specimen. Some signals generated by inelastic

events are: auger electrons, secondary electron, and characteristic x-rays. A secondary electron is thus an electron of an atom of the specimen that has been knocked from its orbit. From these secondary electrons the main image can be formed. The amount of secondary electrons produced will depend on the accelerating voltage (keV) of the beam. Increased accelerating voltage is thus used for elemental analysis where a smaller accelerating voltage gives greater topographical analysis.

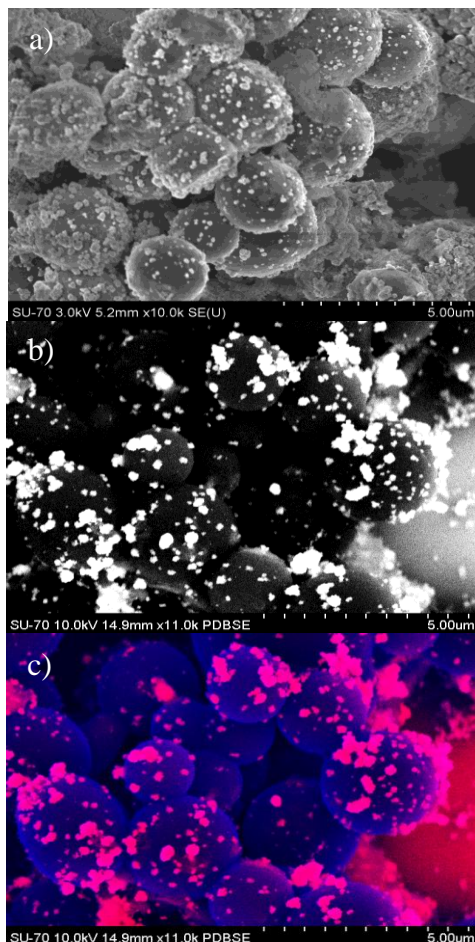


**Figure 2.2** SEM secondary electron detector in a) 3kV b) elemental mapping EDX at 10kV and c) false colour elemental mapping of image b) with carbon highlighted in blue and zinc highlighted in pink.

Due to the SEM's ability to produce inelastic secondary electrons compositional analysis of a sample is possible due to the electrons interaction with the atoms in the sample emitting X-rays of a characteristic

wavelength. This analysis is known as EDX or EDS (energy detection system). One example of the use of such a technique was through the elemental mapping of zinc oxide particles on carbon spheres used in the creation of a double roughness effect as seen in Figure 2.2. The use of elemental mapping allowed the clear visual distinction and identification between carbon and zinc particles in the image indicating the formation of discrete zinc particles on the surface of the carbon spheres in this case. These zinc particles did not prove successful in the formation of a superhydrophobic surface due to poor particle coverage of the spheres but have been used as an illustration of EDX analysis.

## **2.2 Contact Angle Meter**

The contact angle meter used for the measurement of contact angle and contact angle hysteresis was a KSV Cam 200 series, CAM 200 uses drop shape analysis for determining static or dynamic contact angles, absorption and surface/interfacial tensions of liquids. A CCD firewire camera (512x480) with telecentric zoom optics combined with cold lit LED based background lighting allows capturing images (image area  $5.7 \times 5.4 \text{ mm}^2$ ) at frame intervals from 10 ms to 1000s. The contact angle meter was retrofitted with a New Era Pump Systems Inc. NE-1000 Series automated syringe pump for accurate flow rate and volume measurements. Ultrapure deionised water was used as the liquid for all measurements. The KSV contact angle instrument is depicted in Figure 2.3 with standard manual syringe.



**Figure 2.3** KSV Cam 300 Series with high resolution camera and adjustable stage attachments used for the measurement of contact angle and contact angle hysteresis.

As described previously in chapter one, contact angle,  $\theta$ , is a quantitative measure of the wetting of a solid by a liquid. The contact angle instrument was thus used to measure the geometry of the angle formed by a liquid at the three-phase contact line at the liquid, solid and gas interphases. The contact angle is thus determined by the angle between the solid and the tangent to the drop profile at the intersection point. Contact angles were calculated using a Young-Laplace fitting model which fits the shape of the drop accurately by using all of the points on the drop profile with the tangent assigned as the gradient where it intersects the baseline. This is seen to be a more accurate contact angle fitting model as compared to other models such as the polynomial fitting, spherical approximation, axisymmetrical drop shape analysis and analytical approximation solution. The Young-Laplace equation was also used for the determination of contact angle hysteresis.

## 2.3 Contact Angle Hysteresis

Contact angle hysteresis is defined as the maximum advancing and minimum receding contact angles. It can be used to determine the surface heterogeneity, roughness and the mobility of a liquid drop on the surface. Contact angle hysteresis was determined through the dynamic determination of the advancing ( $\theta_a$ ) and receding ( $\theta_r$ ) contact angles. Two main approaches are taken in the calculation of contact angle hysteresis; the first is use of a tilting platform where the sessile drop formed on the surface is tilted until gravitational forces exceed that of the work of adhesion of the drop to the surface where the drop rolls off. The time at which the drop is stable just before the drop rolls off on the advancing side of the drop (downhill side) can be recorded as the advancing contact angle with the receding side (uphill side) of the drop with the difference between these used to determine contact angle hysteresis. This is shown below in Figure 2.4 c). Another method for the calculation of contact angle hysteresis is through the formation of a small sessile drop on the surface of the material to be tested. From this drop liquid is added to the drop until the surface free energy barrier is overcome at the three phase contact line and the droplet diameter transitions to larger surface area with an increased contact angle. The new stable contact angle is then taken as the advancing contact angle. This is depicted below in Figure 2.4 b). Receding contact angle is then determined with the quantitative removal of liquid from the surface of the drop until a similar transition in surface diameter occurs with a reduction in the size of the diameter of the drop and a constant smaller contact angle is produced. This contact angle is then taken as the receding contact angle and is depicted below in Figure 2.4 a). The difference between the advancing ( $\theta_a$ ) and receding ( $\theta_r$ ) contact angles is then taken as the contact angle hysteresis.



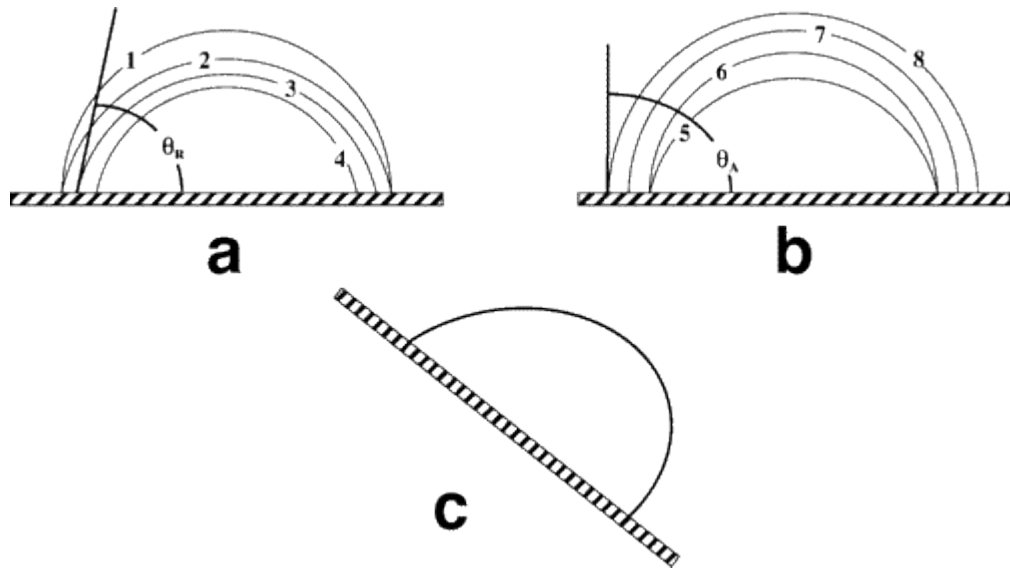


**Figure 2.4** Droplet of water receding on a surface due to evaporation; the droplet is pinned at the three-phase contact line until  $\theta_R$  is reached at 2 and  $\theta_R$  remains constant during subsequent evaporation. (b) A droplet of water advancing on a surface due to quantitative addition; the droplet is pinned at the three-phase contact line until  $\theta_A$  levels at 6. (c) A droplet of water sliding on an inclined surface.<sup>28</sup>

The hysteresis of the sample can then be used to determine the wetting state of the material. The material can have both low hydrophobicity and contact angle hysteresis but in order to be classed as a superhydrophobic material it must possess contact angle above  $150^\circ$  and contact angle hysteresis below  $10^\circ$ . The hysteresis is more relevant in describing the homogeneity of both the surface chemistry and topography. Surfaces with large hysteresis tend to contain both large fractions of both hydrophobic and hydrophilic components and thus contact angle hysteresis is a reflection of the activation energy required for movement of a droplet from one metastable state to another on a surface.

### 3 Experimental

With knowledge of the parameters necessary for the formation of the next generation superhydrophobic material it is the aim of this work to produce a durable large-scale production of a functionalised material with high water repellency and low contact angle hysteresis which is low cost and easy to fabricate. A low cost route to the manufacture of a superhydrophobic material was seen in the production of colloidal particles due to their relative ease of fabrication. Although polymer materials are of low surface free energy and easy to design complex structures for the fabrication of hierarchical rough surfaces they contain some inherent drawbacks. Such drawbacks include their short lifespan, due to their mechanical erosion and heat degradation, and their instability with exposure to acids, bases, and U.V irradiation from sunlight. The use of an inorganic based material would thus provide an inert building block for the production of superhydrophobic materials. The use of an environmentally friendly fabrication of a benign material would also give a competitive edge and a sustainable platform for the production of a superhydrophobic material. Supercritical carbon dioxide was thus used as the medium for the production of a carbon based nanomaterial for use as a superhydrophobic building block material. Below is a detailed account of the experimental steps taken for the production of a self-cleaning superhydrophobic surface with a contact angle above  $150^\circ$  and low contact angle hysteresis below  $10^\circ$  as outlined in the specification for self-cleaning materials.

### 3.1 Supercritical Carbon Dioxide Nanoparticle Formation

The fabrication of an inorganic starting material for the creation of a durable, self-cleaning coating was to be created from the formation of carbon based particles through the use of sc-CO<sub>2</sub> as an environmentally friendly solvent. From what was learned from the production of other colloidal self-cleaning coatings, the use of mono-disperse or almost mono-disperse particles was essential for the fabrication of large scale colloidal assemblies. It was thus decided that the reproducibility of the method would be fundamental towards a self-cleaning material. This was a major initial focus of the project with each parameter changed in order to determine its effect on the process. The method that was used for the production of carbon particles was the use of sc-CO<sub>2</sub> as an environmentally benign solvent and reaction medium. The precursor that was selected and previously shown by Barrett et al.<sup>84</sup> for the production of carbon spheres was squalane. The proposed method of formation of spheres involved the synthesis of colloidal carbon spheres through the carbonisation of squalane micelles at a temperature of 550°C and pressures of 1500-7500psi of sc-CO<sub>2</sub> with reactions carried out in a 120ml, 316 stainless steel high pressure reaction cell. All chemicals were used as received. The non-volatile solvent, Squalane (99.8%) was received from Sigma-Aldrich. All experiments were conducted using liquid withdrawn carbon dioxide from BOC (99.85%) with all high pressure reaction vessels and stainless steel tubing and connections supplied from High Pressure Equipment Company (HiP). Pressure regulation of the CO<sub>2</sub> was controlled by a Teledyne model 260D computer controlled syringe pump and used in-line as shown in Figure 3.1. All experiments were conducted within an Applied Test Systems Inc. model 3210 3-zone heating furnace which allowed for the regulation of temperature to an accuracy of  $\pm 5^{\circ}\text{C}$ .

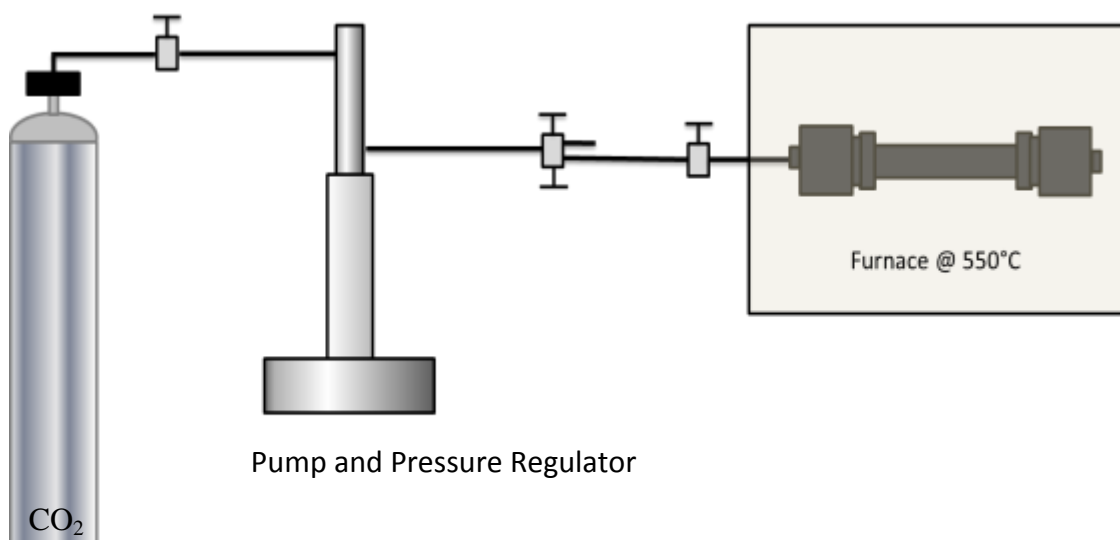


**Figure 3.1:** Schematic representation of the supercritical CO<sub>2</sub> synthesis setup.

Initial parameters set-out for the production of carbon spheres, although capable of producing spheres of appropriate size was limited in its ability to reproduce these results on a continual basis. The initial focus of the work was thus the control of the synthesis of carbon particles in a reproducible fashion with a focus on controlling the size of particles within the process.

### 3.2 Metal Evaporation

A Sigma Instruments SQC 310 Deposition Controller high vacuum thermal evaporator was used for the evaporation of metals onto the surface of preformed assembled carbon sphere layers on a silicon wafer. Both evaporator and metals were stored in an argon filled glovebox to avoid exposure to oxidation. Metals used for evaporation were 99.95% pure 1/8" diameter X 1/8" long pellets were received from

Kurt J. Lesker Company. Metals were evaporated at  $\times 10^{-6}$  bar in a tungsten elong dimple evaporation boat.

### 3.3 Contact Angle

Contact angle measurements were conducted on a KSV Cam 200 series. Ultrapure deionised water was used as the liquid phase for all experiments. A manual syringe was used for all initial static contact angle measurements. A  $10\mu\text{l}$  drop was placed on the surface of the material to be analysed. Measurements were recorded in triplicate on different areas of the substrate. A software programme was used to fit a Young-Laplace model to the drop for the determination of contact angle and contact angle hysteresis. The camera was programmed to record at 1 frame per second (fps) for a total of ten seconds. Contact angle was then determined when a steady sessile drop was formed on the surface of the substrate.

For the determination of contact angle hysteresis an automated syringe pump was retrofitted to the contact angle instrument. The pump was set at a flow rate of  $10\mu\text{l}.\text{min}^{-1}$ . The syringe tip was placed on top of the drop slightly impinging on the drop to allow a steady flow of liquid to flow into/out of the drop as shown on Figure 3.2.

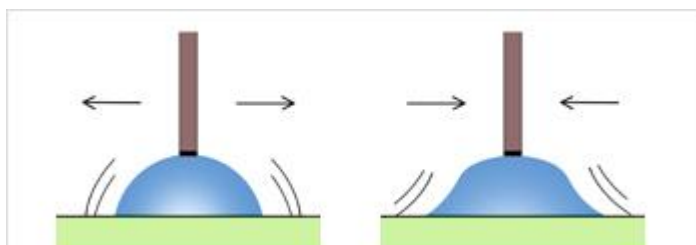


**Figure 3.2** The principle of the dynamic contact angle measurement.

A small drop was allowed to form and was allowed to come in contact with the substrate through reducing the distance between the drop and the substrate. Image

recording was set at 100fps and the pump allowed to run thus increasing the volume of the drop for the determination of advancing contact angle ( $\theta_a$ ). The pump was then set to withdraw the liquid at the same rate and from this the receding contact angle ( $\theta_r$ ) was determined. Advancing and receding contact angles were determined with the same computational fitting as the static contact angle.

## 4 Results and Discussion

Initial work carried out on the tailoring of the process involved the isolation of the nucleation and growth phases in time during sphere synthesis. For this a study on the effect of change in parameters such as temperature, pressure, heating rate, and synthesis time was performed on the growth of spheres during synthesis. SEM images of spheres produced from a typical initial “poor” synthesis are shown in Figure 4.1 within a range of 550°C (a & b) and 450°C (c & d). The spheres produced can be seen to be polydispersed in size ranging anywhere from approximately 1 - 4µm. Sphere shape ranged from spherical to oblong in shape, with necking of spheres seen at elevated temperatures (a & b), causing the formation of non-uniform structures which is undesirable for colloidal assembly.

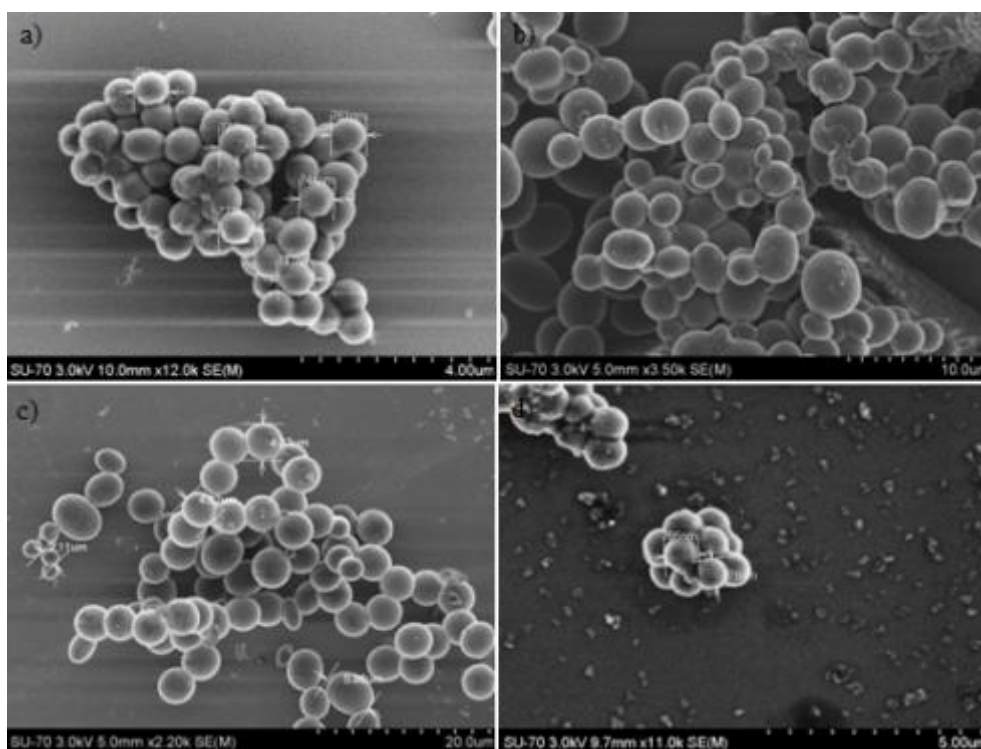


**Figure 4.1** SEM images of carbon spheres synthesised at 550°C, 5500psi for 45 minutes a&b and carbon spheres synthesised at 450°C, 5500psi for 45 minutes c&d.

The results seen in Figure 4.1 suggest that at elevated temperatures two or more nucleation and growth stages are occurring during synthesis of the carbon spheres. Lower temperatures produce more monodisperse spheres with incomplete synthesis occurring at temperatures below 450°C. This analysis shows however that carbon spheres are capable of being synthesised at varying temperatures which may be beneficial for further modification of the spheres.

Through careful and deliberate modification of each parameter, it will be shown that no one parameter has a designated effect on sphere formation. Control of the system was only seen when more than one parameter was changed in a single reaction from the initial synthesis parameters of 550°C, 5500psi and 45 minutes.

#### **4.1.1 Temperature Programme**

With the formation of carbon spheres seen through the thermal decomposition of squalane, a study on the effect of temperature was carried out with the ramp rate and final temperature varied to determine their effect. The furnace control setup used is shown in Figure 4.2. The ramp rate selected was broken into three separate stages, allowing for nucleation and growth to occur separately as per the La Mer particle growth principle. Stage one of the temperature programme involved the rapid ramp in temperature from room temperature to 300°C. This step was taken to allow for a rapid controlled burst in nuclei for the formation of particles. The quicker and more controlled this stage of the temperature programme the more monodisperse the carbon spheres. Stage two of the temperature programme involved the ramping of temperature up to the desired end temperature. The temperature was ramped at a rate of 1°C/min. It was shown from experimentation



that this ramp rate gave the most consistent size distribution as compared to other ramp rates of 0.5, 2, 3, 4, and 5°C/min.

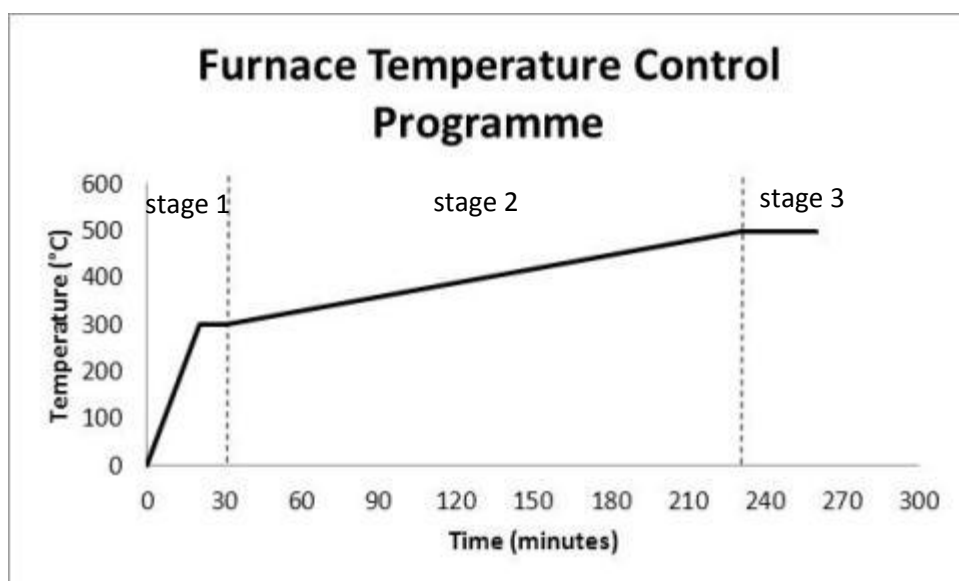


**Figure 4.2** Three zone furnace temperature programme for synthesis of carbon spheres.

Stage three of the temperature programme was set as a holding step to ensure the complete use of the Squalane precursor during synthesis. This stage was incorporated to ensure that all monomer was used during the particle growth phase. From this analysis it was seen that a finite range of temperature along with a slow controlled ramp rate was seen to give the most favourable results. The use of this temperature programme at 1°C/min. was used for further analysis of parameter effects as it gave reproducible results which allows for the direct comparison of parameter changes. The spheres produced with the temperature programme at 1°C/min. can be seen in figure 4.3. These spheres although not perfectly monodisperse show great improvement in the tailoring of the system as compared to initial system setup as shown with the spheres produced in Figure 4.1.

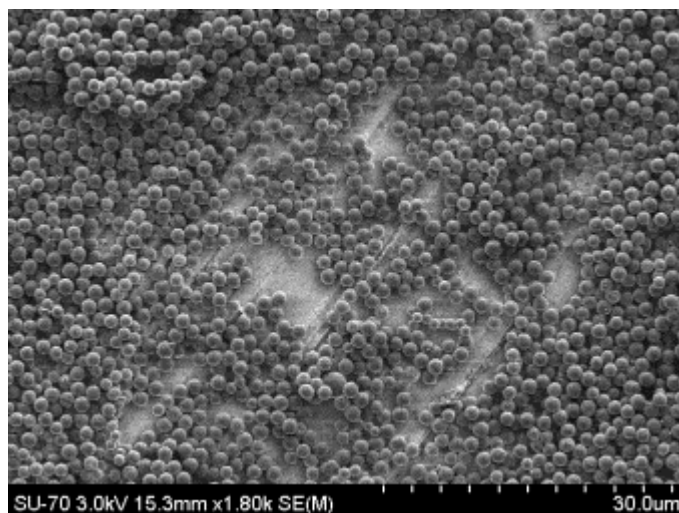


**Figure 4.3** SEM image of carbon spheres synthesised with temperature programme at 550°C, 5500psi at a ramp rate of 1°C.min<sup>-1</sup>.

#### 4.1.2 Effect of Temperature on the System

With the ability to reproducibly produce spheres of the similar size and shape, it was now possible to directly compare the effect of temperature on the system. The final temperature reached for stage three of the temperature programme was run at three different temperatures 480°, 500°, and 520° with the results at 550° being the base comparison temperature. Figure 4.4 shows how a change in final temperature using the furnace temperature programme shown in Figure 4.2 has a dramatic effect on carbon sphere size and monodispersity produced. Figure 4.4 a & b show the spheres produced from a final reaction temperature of 480°C. From these SEM images it can be seen that sphere size is controlled to approximately 1.4µm. A further reaction was subsequently run with temperature increased to 500°C. Particle size was seen to remain unchanged with this increase in temperature. The main difference that was noticed with replications of these experiments was that samples prepared at 500°C produced “cleaner” spheres than the reaction at 480°C. It was

determined that the reaction at 480°C displayed incomplete formation of spheres, evident by inorganic debris seen on and around the spheres in Figure 4.4 a). An increase in temperature from 500°C to 520°C consistently produced spheres polydisperse in size. Spheres can also be seen to be necked in Figure 4.4 e & f. This may be a possible cause for polydispersity with aggregation of particulates at elevated temperatures creating larger particles.

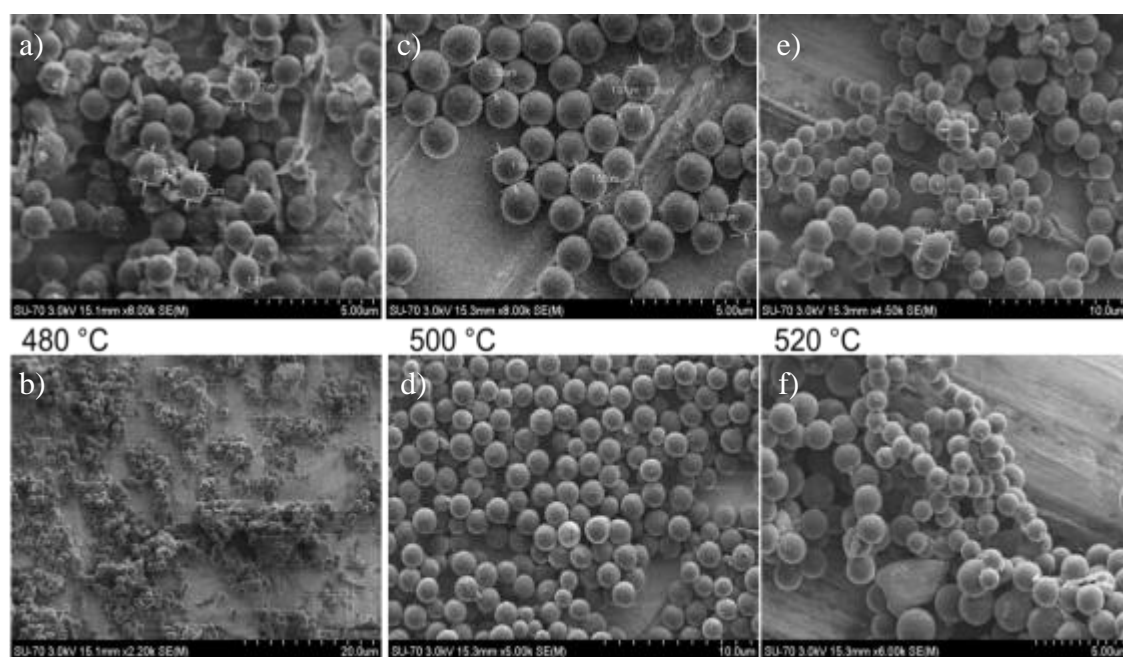


**Figure 4.4** SEM images of the temperature study performed on carbon sphere formation.

From this work it was seen that spheres could be reproducibly synthesised to a size of approximately 1.4µm. All further work incorporated the temperature programme above with a reduced reaction temperature of 500°C as these parameters produced the most reproducible particle size and morphology.

### 4.1.3 Effect of Pressure on the System

Carrying on from this temperature study, a study on the effect of pressure was carried out using the new optimised synthesis setup. The initial pressure of the sealed vessel was varied from 4,500 to 5,500psi at 500°C.

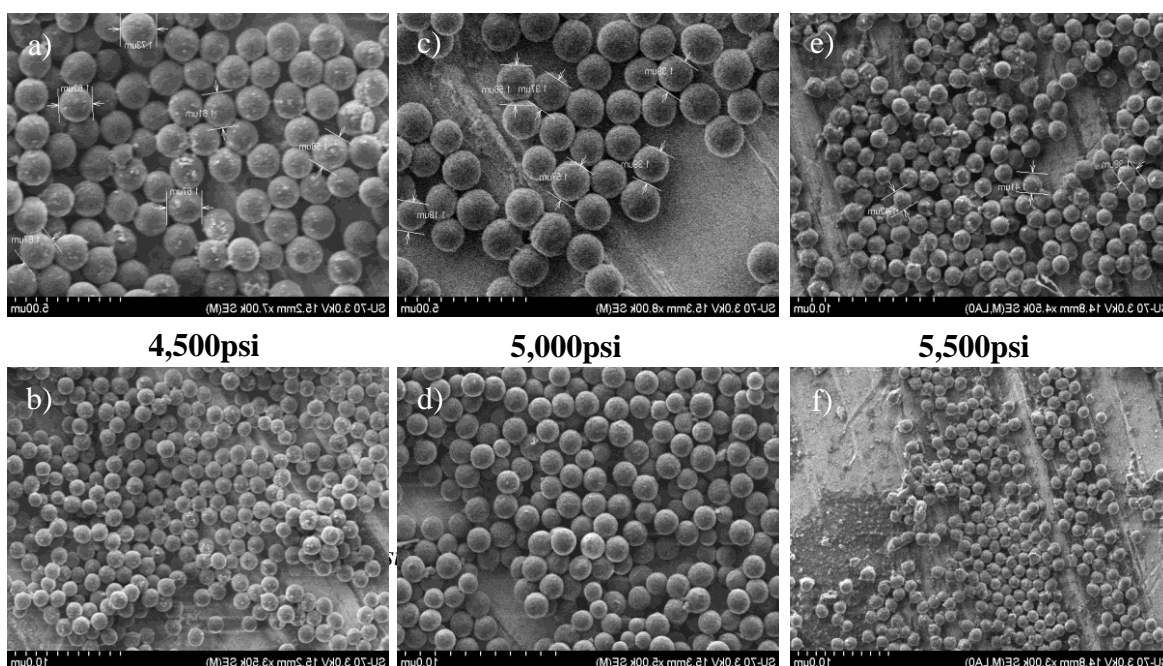


**Figure 4.5** improved synthetic method of carbon spheres. All spheres were synthesised at 500°C in a 4.5hr reaction. Image a) and b) show a typical batch of spheres produced at 4,500psi, c) and d) a reaction run at 5,000psi with e) and f) displaying images of a reaction run at 5,500psi.

It was seen in all reactions involving pressure modulation, that no correlation between pressure and size of particles was seen under these synthetic conditions. From images in Figure 4.5 a) to f) all spheres ranged from 1.4 – 1.5μm in size, with no definite linear relationship seen in the increase or decrease in size, dependent on pressure. Pressure was increased up to the maximum pressure output from the Teledyne model 260D computer controlled syringe pump of 7,500psi. With this increase in pressure no obvious decrease in size of particles was seen, showing no relationship between particle size and system pressure in this altered synthesis setup.

#### 4.1.4 Squalane Injection Volume Study

A study of the effect on how the volume of squalane (injected prior to reaction) affected the morphology of the carbon spheres was also studied. The volume of squalane injected into the reaction vessel (120cc) was altered from 0.2ml (0.667%) to 1.5ml (1.25%) of squalane, with all other parameters constant at 500°C and 5000psi. It was found from this study that the size of the spheres directly correlated with the volume of squalane injected. From Table 4.1 it can be seen that the size of the spheres could be reduced down to an average particle size of approximately 1µm with monodisperse particle formation. The larger the volume of squalane injected the more monomer available for the formation of larger spheres. With increased volume of squalane up to 1.5ml, more polydisperse spheres were seen to be formed. This may have been as a result of sufficient monomer being available for multiple nucleation bursts to have occurred and thus particle growth occurring at different rates during the synthesis of spheres resulting in polydispersity.

Particle flocculation during the growth or nucleation stages due to increased precursor availability may also account for the noted increase in size and polydispersity of particles with increased volumes of squalane. Reducing the volume of squalane could reduce the potential of collisions and coagulation of particles in the sc-CO<sub>2</sub> solvent during synthesis. With further scale-up of the process this flocculation could be overcome with the increase in volume of the reaction vessel.

**Table 4.1** Relationship between volume of Squalane injected and particle size of carbon spheres synthesised.

Volume of Squalane Injected (ml)	Average Particle Diameter ( $\mu\text{m}$ )
0.2	1.05
0.3	1.1
0.4	1.4
0.5	1.5
1.0	1.8
1.5	1.8

#### 4.1.5 Summary of Optimisation

From the reaction studies carried out, three parameters were seen to be important in the synthesis of monodisperse carbon spheres. Firstly, the use of a ramping temperature programme allowed for the separation of nucleation and growth of the particles. The temperature at which the reaction was carried out was also seen to affect the resultant sphere formation with the reduction in synthesis temperature from 550°C to 500°C showing more complete sphere formation with less necking of particles and greater monodispersity. The volume of squalane injected was also seen to affect the synthesis of the spheres, with a reduction in volume from 1.0ml to 0.3ml seen to reduce sphere size.

Parameters where a reduction in particle size or an increased monodispersity of particles was seen were thus taken as the optimised synthesis conditions of the carbon spheres with greater repeatability of particle growth. All further reactions were subsequently done at these optimised conditions 0.3ml of squalane at 500°C and 5000psi ran in accordance with the temperature ramping programme in Figure

4.2, resulting in the formation of almost monodisperse carbon spheres of approximately 1.0 $\mu\text{m}$  as seen in Figure 4.6 below.

#### 4.1.6 Contact Angle of Carbon Spheres

For analysis of the contact angle of the carbon spheres, a layer of roughly 1 $\mu\text{m}$  spheres were deposited onto the surface of a silicon wafer (Figure 4.6). The contact angle of the silicon wafer was predetermined through the use of the contact angle instrument to be approximately 33°. The creation of a uniform and complete layer of carbon spheres was thus essential for an accurate determination of contact angle on the surface of a deposited layer of carbon spheres.

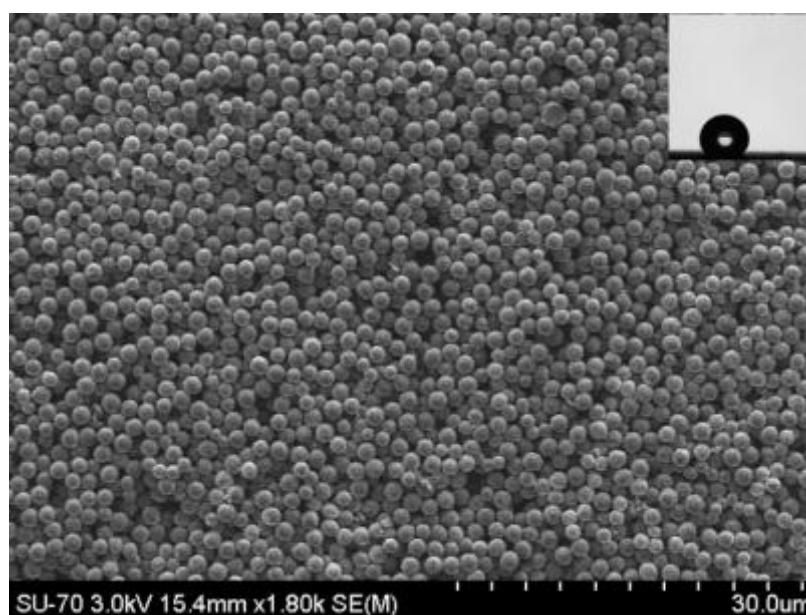


**Figure 4.6** SEM image of deposited layer of carbon spheres with insert of water contact angle.

The as-prepared carbon sphere layer gave a typical water contact angle of approximately 140°. This large contact angle showed the hydrophobicity of the layer produced. These spheres however did not display superhydrophobicity which was needed for the creation of a self-cleaning material. In order to determine the

interaction of the drop with water, the dynamic contact angle of the spheres needed to be calculated. This was achieved through the determination of the contact angle hysteresis of the deposited carbon layer.

#### **4.1.7 Contact Angle Hysteresis of Carbon Spheres**

The contact angle hysteresis of the carbon spheres was calculated using the increment/decrement method as described above in Section 2.3. The hysteresis of the carbon sphere sample was expected to be large as the drop was not seen to be free to roll on the surface of the substrate. The advancing contact angle was taken when the water droplet placed on the surface of the carbon spheres increased in base line diameter as circled in Figure 4.7 b). The equivalent point is circled in Figure 4.7 a) and is taken as the advancing contact angle of  $131.0^{\circ}$ .



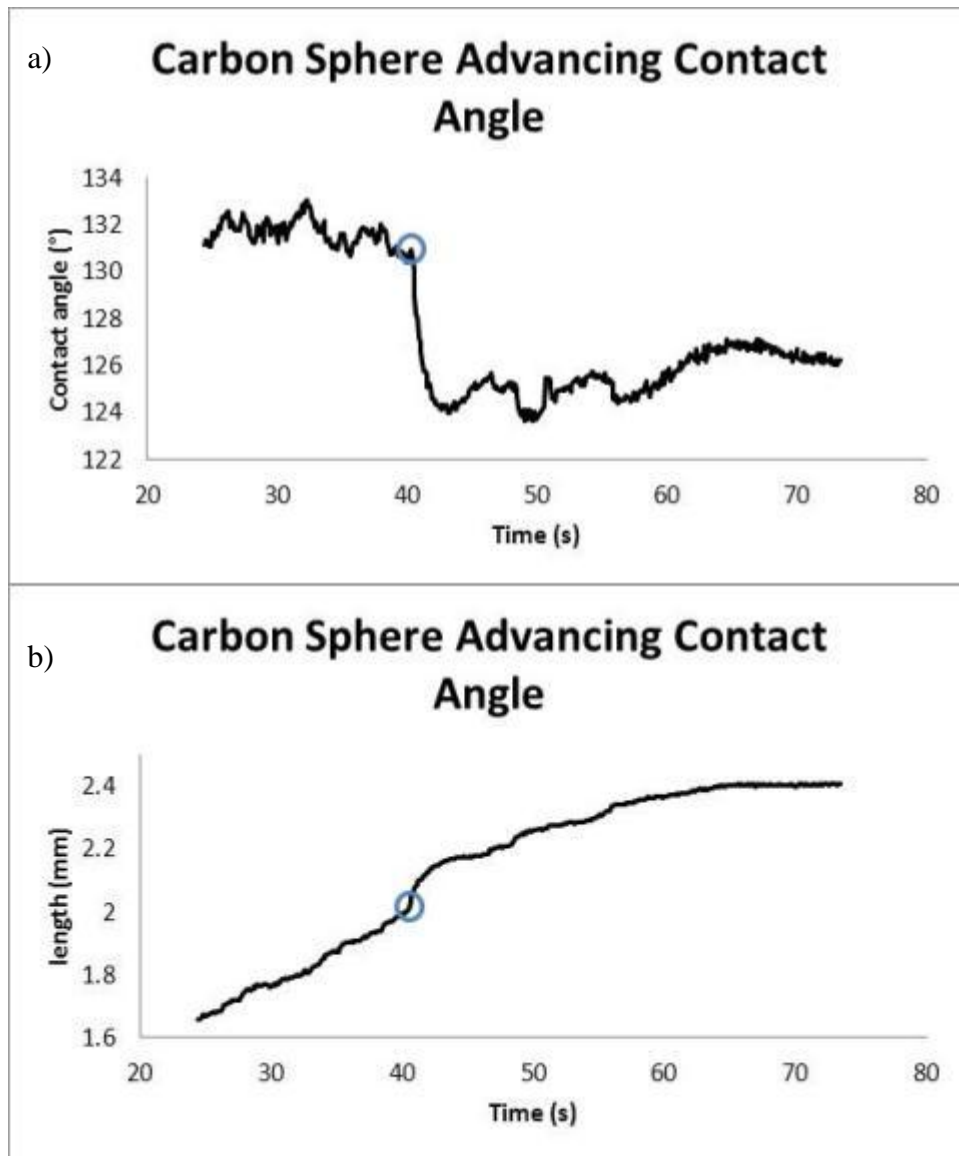


**Figure 4.7** a) Contact angle measurements of a water droplet advancing across a layer of carbon spheres and b) the same water droplet's base diameter.

The drop was then allowed to equilibrate on the surface of the carbon spheres and the volume of the drop reduced through the removal of water using a syringe needle. The drop was seen to recede slowly across the substrate with no depinning event. The lowest contact angle measured was at 62.2° from Figure 4.8. The contact angle hysteresis of the material was subsequently calculated with an advancing contact ( $\theta_a$ ) angle of 131.0° and receding ( $\theta_r$ ) of 62.2°, the contact angle hysteresis of the

layer of carbon spheres can thus be determined to be  $(\theta_a)$  minus  $(\theta_r)$ , therefore contact angle hysteresis is equal to  $68.8^\circ$ . The real contact angle hysteresis of the material is probably larger than this calculated figure as the drop has seen to be physically adhered to the substrate through  $180^\circ$  rotation.

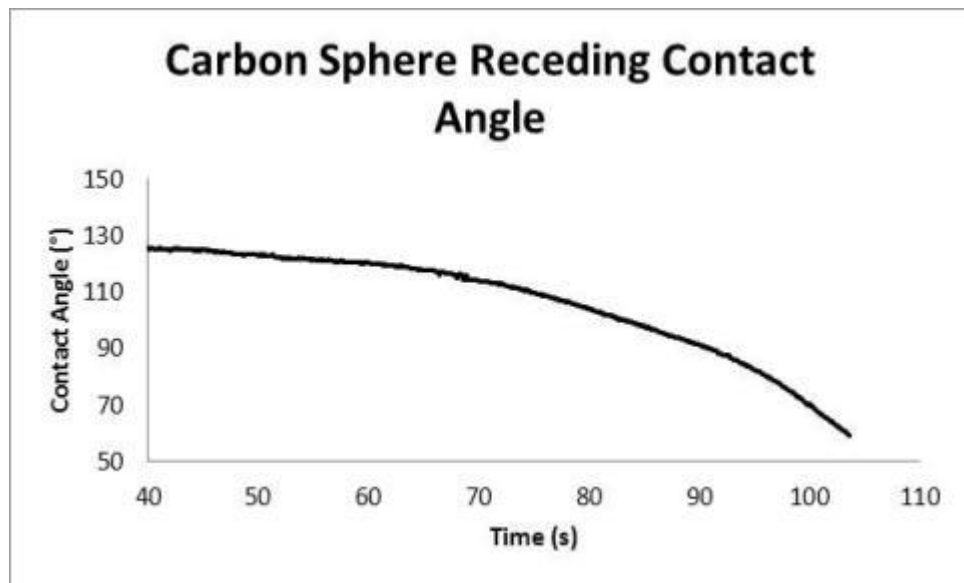


**Figure 4.8** Contact angle measurements of a water droplet receding across a layer of carbon spheres and

This large hysteresis of the as deposited carbon sphere films shows that although the surface created is hydrophobic, self-cleaning of the surface of the material through contact with water would be impossible under normal working conditions. For the creation of a superhydrophobic self-cleaning material, functionalization of the carbon spheres would be necessary for the creation of a Cassie-Baxter state wetting regime on the surface of the film, as compared to the Wenzel type wetting currently seen on the film through the large contact angle hysteresis. For this, a dual-

scale hierarchical roughness would need to be created with the formation of nanoscale roughness on the surface of the spheres.

## **4.2 Roughening of the Carbon Spheres**

From previous work on controlling the growth of carbon spheres and the hydrophobicity and hysteresis seen due to the chemical composition and structure of the particles, it was now the aim of the project to increase this hydrophobicity and to lower the hysteresis to produce a superhydrophobic self-cleaning material. The goal of this section of the work was thus to achieve contact angles with water above  $150^\circ$ , with contact angle hysteresis below  $10^\circ$ . This was to be achieved through the reduction of surface area in contact with the impinging water droplet through the roughening of the carbon sphere surface. Roughening of the surface has been discussed previously in depth in Chapter 1 and has been shown to dramatically increase contact angle in related studies<sup>49, 50, 97</sup>. The approach taken to increase surface roughness of the carbon spheres was to evaporate thin nanometre thick metal layers onto the surface of the spheres which grow through Volmer-Weber, or island growth formation.<sup>72</sup> Through the growth of nanometre sized islands on the surface of the carbon spheres a dual-scale hierarchical roughness could be created to mimic the surface seen on the lotus leaf. Through careful layer formation of the spheres and subsequent metal evaporation, it would be possible to create an all-inorganic based hard-wearing and durable superhydrophobic self-cleaning coating.

### **4.2.6 Evaporated Titanium**

Initial work performed on the evaporation of metals was conducted through the use of Ti as a metal for the formation of islands on the surface of the carbon spheres.

Figure 4.9 a, b, and c, shows a series of increased magnifications of a thin homogenous layer of Ti evaporated onto the surface of the spheres. It is evident from these images that Ti films grow on the surface of the carbon spheres through a Frank-Van der Merwe<sup>72</sup> or possibly Stranski-Krastinov<sup>72</sup> growth mechanism, with surface roughness of only a few nanometres seen on the surface of the evaporated Ti. This “smooth” deposition is indicative of such growth mechanisms with no island formation seen on the surface of the spheres. Figure 4.9 d) shows the resultant contact angle of  $\sim 114^\circ$  on the as deposited Ti 20nm layer on carbon spheres. The contact angle of the spheres has seen to be reduced as compared to a layer of as-synthesised carbon spheres. The contact angle is greater however than an evaporated 20nm layer of Ti (approximately  $60^\circ$ ), showing the effect of the evaporation of the metallic layer onto the carbon spheres and thus the roughness imparted onto the metallic layer and subsequent increase in water contact angle. This is a similar result as compared to the work of Cheng et al<sup>39</sup> when studying the lotus leaf, they saw a reduction in contact from  $126^\circ$  on the annealed surface of the lotus as compared to a flat carnauba wax with a contact angle of  $76^\circ$ , used to simulate the chemical characteristics on the surface of the leaf. This reduction of  $50^\circ$  in contact angle due to the microscopic roughness on the surface of the lotus leaf can be compared to the increase in contact angle of approximately  $45^\circ$  seen from evaporating a Ti layer onto carbon spheres as compared to a smooth surface. This displays the similarity and effectiveness of the carbon spheres and their ability to mimic the roughness on the surface of the lotus leaf. This result, although not a positive result in terms of contact angle, shows the potential of the carbon sphere layer for the creation of a superhydrophobic material.

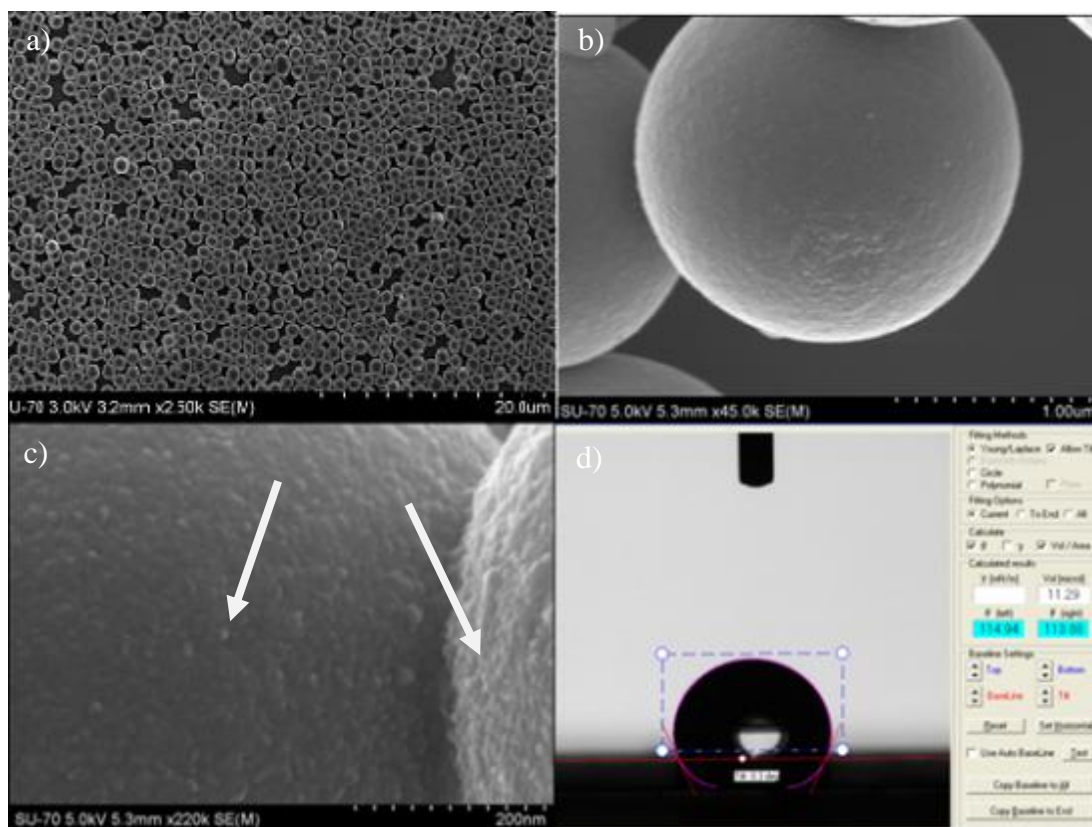


**Figure 4.9** SEM image of Titanium evaporated on the surface of carbon spheres showing a homogenous surface coverage in a) on several spheres and b) on one sphere with a scale bar of 1  $\mu\text{m}$ . Nanosized asperities can be seen in image c) with a scale bar of 200 nm. Image d) is a screenshot of contact angle measurements performed on a layer of carbon spheres coated with a 20 nm layer of evaporated Titanium.

#### 4.2.7 Evaporated Aluminium

Carrying on from the work of the evaporated Ti and encouraged by the increase in contact angle of evaporated Ti on carbon spheres, as compared to a “smooth” 20 nm evaporated Ti layer, other metals were evaporated onto the surface of the carbon spheres. Al was chosen as a possible precursor for the formation of metallic islands on the surface of the carbon spheres. A 20 nm layer of Al was subsequently evaporated, with this thickness selected to encourage incomplete film formation and thus island formation of the metal. This thickness is also biomimic of the surface

roughness of the nanometre sized hairlike structures seen on the surface of the lotus. The resultant surface composition can be seen in Figure 4.10.

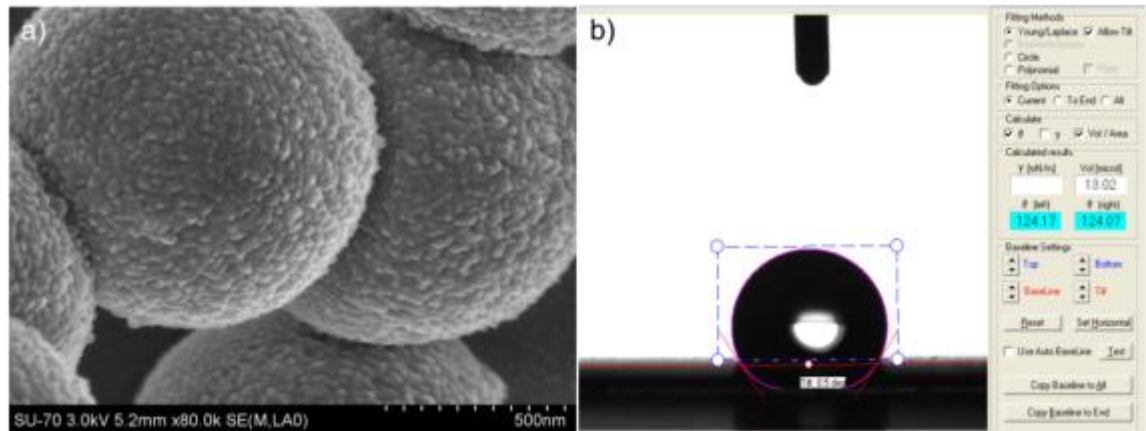


**Figure 4.10** a) SEM image of the carbon spheres with a 20nm evaporated Al layer and b) water droplet creating a contact angle of  $124^\circ$  on the surface.

From looking at image a) in Figure 4.10 it can be seen that the metallic layer deposited on the evaporation of the 20nm layer of Al created a rougher surface on the carbon sphere. The contact angle measurements in figure 4.10 b)( $\sim 124^\circ$ ) shows that although the surface of the spheres is visually “rougher”, the size and height of the roughness is not large enough for the formation of Cassie-Baxter state wetting on the surface with a water contact angle of  $124^\circ$  seen on the evaporated Al layer. This increase in roughness does show an increase in contact angle as compared to that of a smooth evaporated Ti layer.

Although nanometre scale roughness along with submicron scale roughness is evident in this sample, responsible for superhydrophobicity on the lotus, the reduced water contact angle suggests that the size of the nanometre scale roughness is not large enough to support bridging of the water droplet across the asperities on the surface of the carbon spheres.

Although Al and Ti are high surface energy materials<sup>98, 99</sup> it must also be considered that these evaporated metals were 99.98% pure when evaporated onto the surface of the carbon spheres. A native oxide layer will form on the surface of these metals in air. Interactions between water and the surface must therefore be considered as that between water and primarily the oxide  $\text{Al}_2\text{O}_3$  and  $\text{TiO}_2$  respectively. This oxide will therefore increase the hydrophilic portion of the surface in contact with the drop decreasing the water contact angle. With this considered, the use of evaporated Ti and Al layers onto carbon spheres has displayed the ability to use high surface energy metals for use as a hydrophobic material. The use of evaporated Al on the surface of carbon spheres has already surpassed the limitation of the use of smooth low surface energy materials ( $-\text{CF}_3$ -terminated surface) of approximately  $120^\circ$ ,<sup>6</sup> as compared to the evaporated Al of  $124^\circ$ . This displays that the use of all-inorganic materials have the potential as use as hydrophobic surface coatings.

#### **4.2.8 Evaporated Indium**

Monodisperse carbon spheres were taken and deposited onto a silicon wafer. 20nm of In was then evaporated onto the carbon spheres. Figure 4.11 shows the islands of In that subsequently formed on the surface of the carbon spheres. As compared to results from the evaporation of Ti and Al, it is evident that the In layer grew through the formation of discrete islands as compared to a metallic layer with a roughened texture on the surface in the case of Ti and Al.

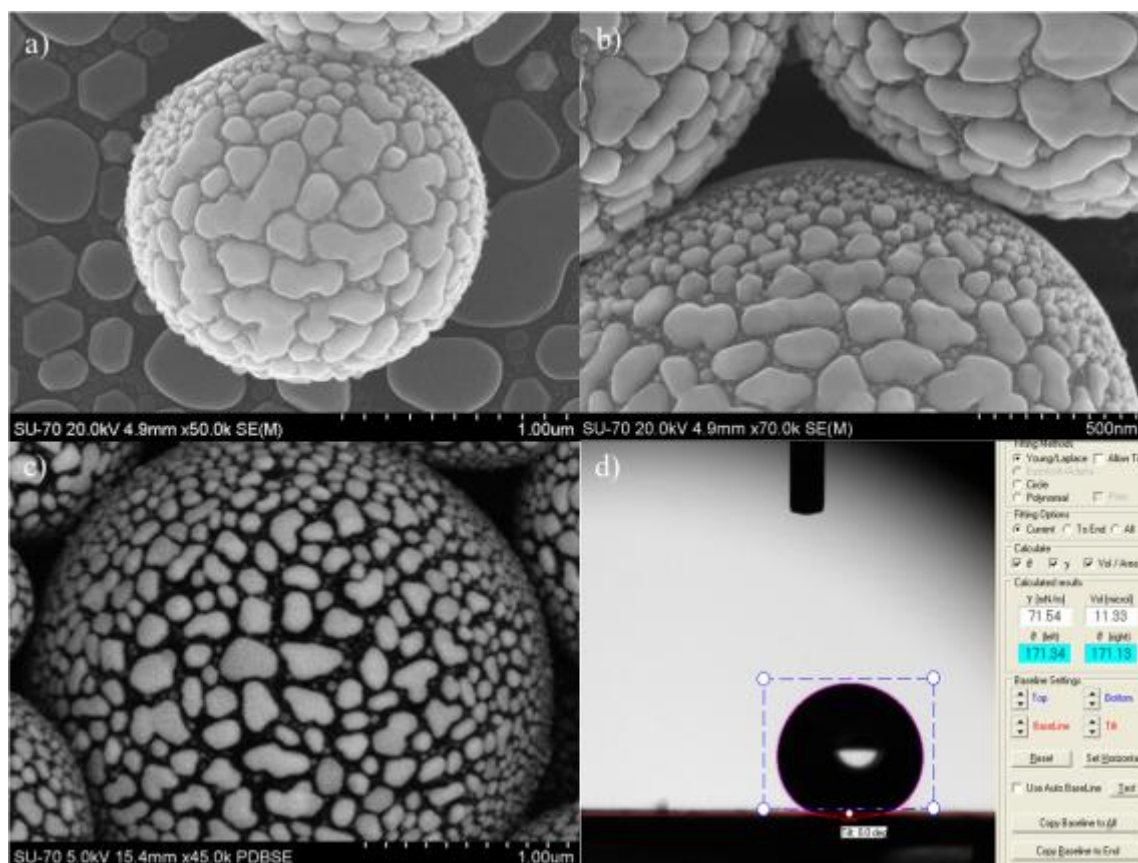


**Figure 4.11** a) SEM image of 20 nm evaporated In on the surface of carbon spheres showing island formation, b) intersection of three spheres tilted at 50° displaying the reduction on particle size on the edge of the sphere, c) backscattered electron detector (BSE SEM), and d) water contact angle measurement of 20nm evaporated In layer on carbon spheres.

Water contact angle analysis performed on the 20nm evaporated In layer displays large contact angles, with a static contact angle of  $>171^\circ$  seen in Figure 4.11 d). The backscattered electron detector (BSE) Figure 4.11 c) used for the collection of elemental analysis displays the discrete In islands, showing brighter due to being a heavier atom, contrasted against the darker, lighter, carbon sphere background. The water contact angle of  $>171^\circ$  shows that the formation of In islands on the surface of the carbon spheres allows for the bridging of the impinging water droplet across the islands. This state of wetting is evident in the Cassie-Baxter state of wetting and is the wetting regime displayed by the leaf of the lotus. The use of evaporated In on the



surface of carbon spheres displays the potential for applications as a superhydrophobic material due to its extremely high water contact angle. To the best of our knowledge this is the first time that evaporated metals on carbon spheres have been used to create such large contact angles.

In order to be classified as a superhydrophobic material however, the surface would have to have a sliding angle below  $10^\circ$ . Prior to the determination of sliding angle and contact angle hysteresis the effect of the evaporation layer on the surface of the carbon sphere was to be determined for its effect on contact angle and contact angle hysteresis. Different layer thicknesses of In were evaporated, ranging from 20, 30, 40, 50, and 100nm. Images of the evaporated layers are displayed in Figure 4.12. The increase in thickness shows a reduction in contact angle from  $171^\circ$  to  $168^\circ$ , with a 10nm increase in layer thickness. A dramatic change in contact angle is then seen with the evaporation of a 40nm layer of In on the surface. It can be seen from Figure 4.12 c) and d) that the distance between the In island asperities is reduced. The islands seem to have coalesced into a more homogenous film, thus reducing the ability of the In layer to support a Cassie-Baxter wetting and thus regress into a Wenzel state of wetting. This is seen to occur within a refined evaporation range from approximately 40 – 80nm. The continued increase in layer thickness up to 100nm sees island formation occur again and thus Cassie-Baxter wetting of the surface is supported once more.

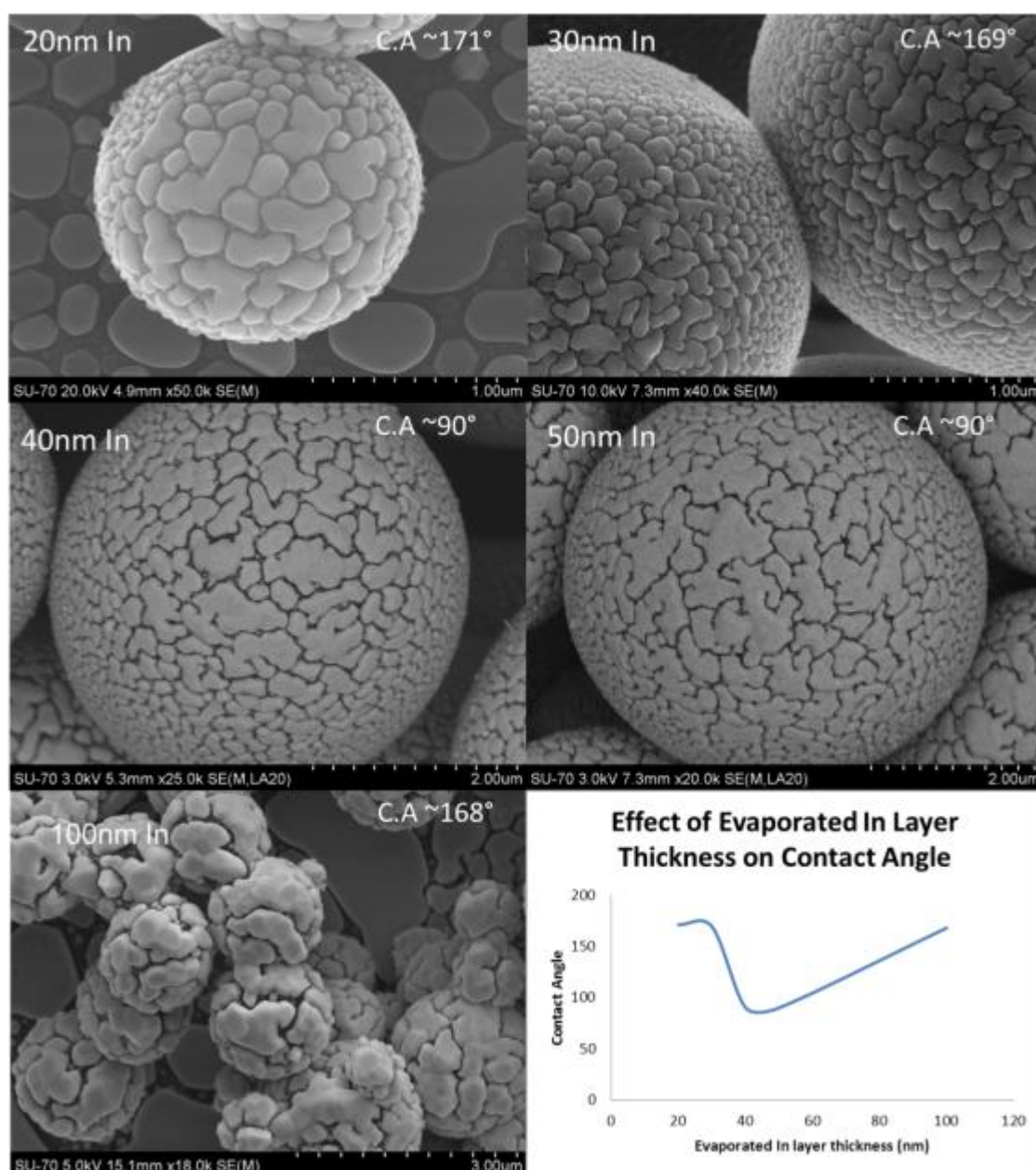


**Figure 4.12** SEM images of a) 20nm, b) 30nm, c) 40nm, d) 50nm, e) 100nm layers of evaporated In with f) graphical representation of the effect layer thickness on contact angle.

In order for the evaporated In on carbon to be classed a superhydrophobic material the sliding angle and contact angle hysteresis of the material needed to be quantified. Initial quantification of the hysteresis of the sample was through the tilting of the substrate and through the determination of the angle at which a drop of water rolled off the surface of the substrate. Figure 4.13 shows a droplet of water at

the moment of rolling on the surface a 20nm layer of evaporated In on carbon spheres. Through the use of the CAM 200 software the sliding angle of the surface was determined to be  $3.5^\circ$ . Figure 4.14 is the moment at which the droplet became unpinned from the surface of the substrate.



**Figure 4.13** Screenshots taken during the tilting of a water form on the surface of an evaporated 20nm layer of In on carbon spheres.

The CAM 200 software was used to determine the tilt or sliding angle specific to the substrate. This meant that through a small inclination of the substrate of  $\pm 3.5^\circ$  water would roll off the surface of the material. This low sliding angle combined with the extremely large contact angle of  $> 171^\circ$  indicated that the evaporated 20nm In layer on carbon spheres displays superhydrophobicity not only mimicking, but greatly exceeding the contact angle of approximately  $160^\circ$  and a sliding angle of  $6^\circ$  calculated on the surface of the lotus leaf.

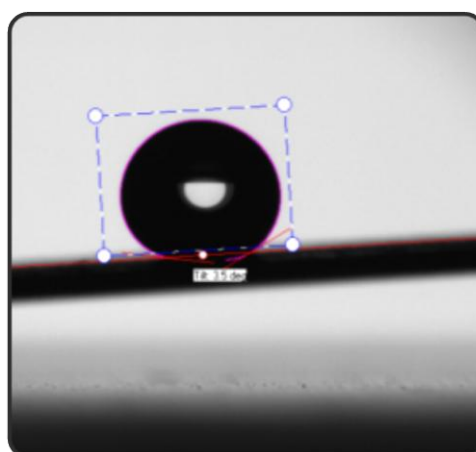


**Figure 4.14** Screenshot of the moment the droplet of water became depinned from the surface of the substrate and thus the subsequent calculation of the sliding angle of the material.

The hydrophobicity of the material synthesised through the formation of a dual scale In on carbon hierarchical surface structure can further be demonstrated in Figure 4.15. The filmstrip shows the first 0.3 seconds of the interaction of the water droplet with the substrate. The drop was dispensed from approximately 1cm from the surface of the material. Due to the extreme hydrophobicity of the material the drop bounces on the surface of the material. The ability of the drop to bounce on the surface of the substrate from such a small distance further demonstrates the formation of a Cassie-Baxter wetting regime on the surface of the material while displaying the extreme water repellency of the material.

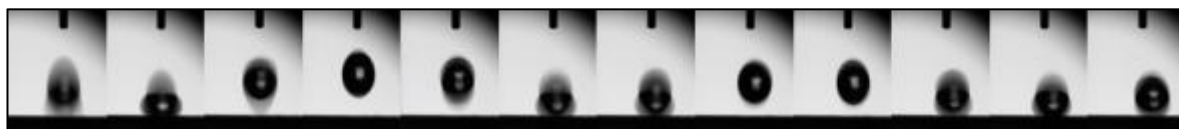


**Figure 4.15** Screenshots taken as a 10 $\mu$ l droplet of water is dispensed from a height of 1cm above the surface of a 20nm evaporated In layer on carbon spheres.

### 4.3 Contact Angle Hysteresis of 20nm Evaporated Indium Layer

Contact angle hysteresis was calculated through the increment/decrement method whereby a small drop of water was carefully placed on the surface of the substrate. The volume of the drop was then increased at a rate of 10 $\mu$ l.min<sup>-1</sup>. The CAM 200 contact angle instrument was set to record at 10fps. The subsequent advancing contact angle was thus calculated from the point at which the drop transitioned from one metastable state to another. This transition can be seen at the point where the diameter of the three phase contact line dramatically increases. This can be physically seen at the point where the droplet “jumps”, advancing outwards across the substrate. The greater the interaction of the water drop with the surface, the larger the gap between the two metastable states and thus the greater the

transition in size between them. The greater the transition results in a larger difference between contact angles and thus a larger contact angle hysteresis. The hysteresis therefore indicates the level of interaction between the impinging water droplet and surface of the substrate. The larger the hysteresis the greater the interaction, thus suggesting a Wenzel wetting regime as compared to the reduced solid fraction in contact with the water drop in a Cassie-Baxter wetting regime.

The data point circled in black in Figure 4.16 indicates the point at which the drop transitioned from a base diameter of 0.407mm to ca. 0.900mm. This jump in base diameter is responsible for the dramatic decrease in contact angle from a maximum of  $175.9^\circ \pm 1^\circ$ . It is this figure that is taken as the advancing contact angle of the material.

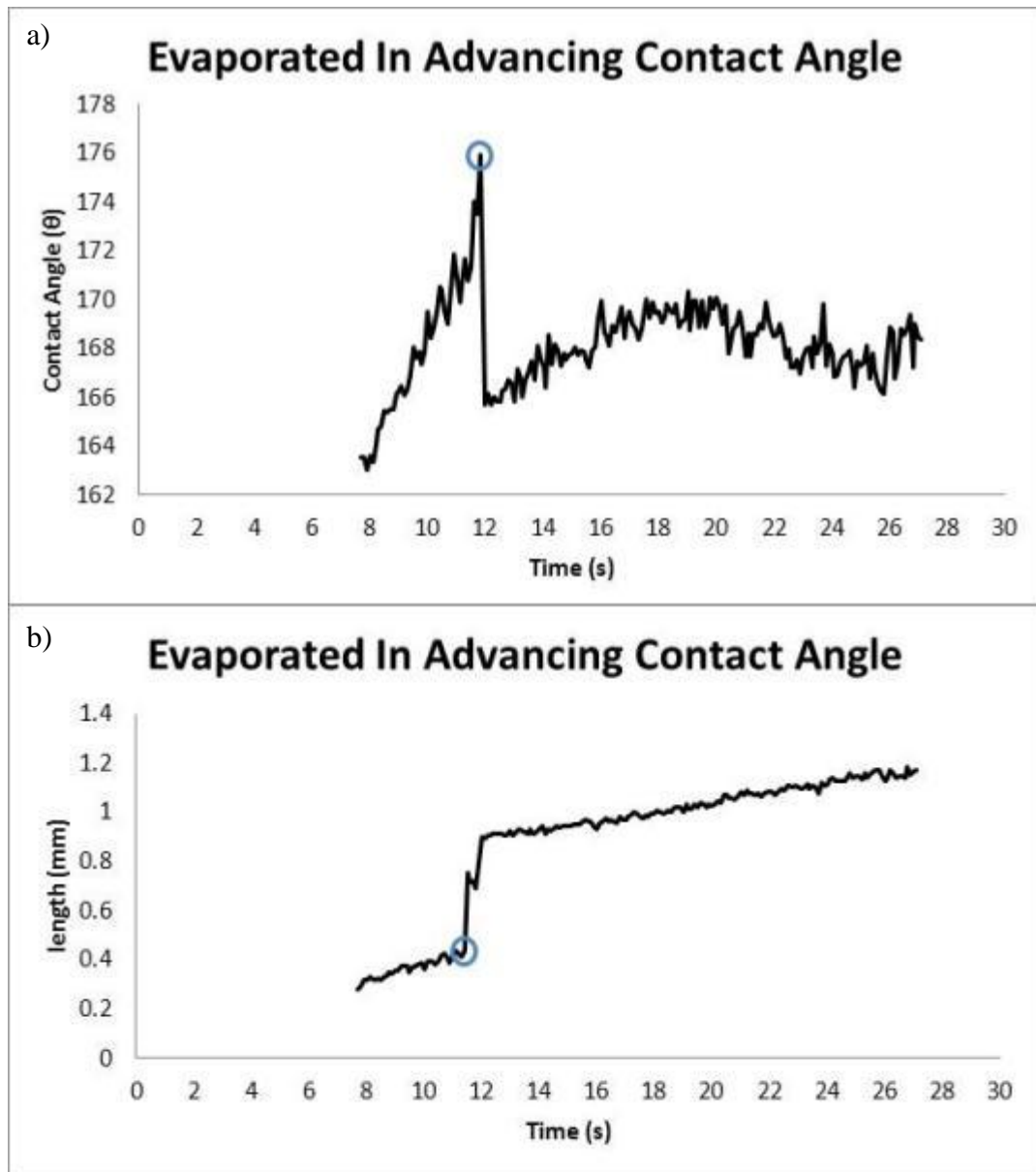


**Figure 4.16** a) Contact angle measurements of a water droplet advancing across the substrate and b) the same water droplet's base diameter.

From this advanced drop the syringe pump motor was reversed and was set to remove volume from the drop at a rate of  $10\mu\text{l}.\text{min}^{-1}$ . Due to the low adhesion of the drop to the surface of the substrate it can be seen from Figure 4.17 that the base diameter of the drop is constantly in motion. This indicates that the drop is almost free to move on the surface of the substrate. It was therefore taken that the first

transition in base diameter of the drop was taken as the receding contact angle, as indicated by the black circle in Figure 4.17. This transition in base diameter of the drop relates to a contact angle of  $171.8^\circ$ .

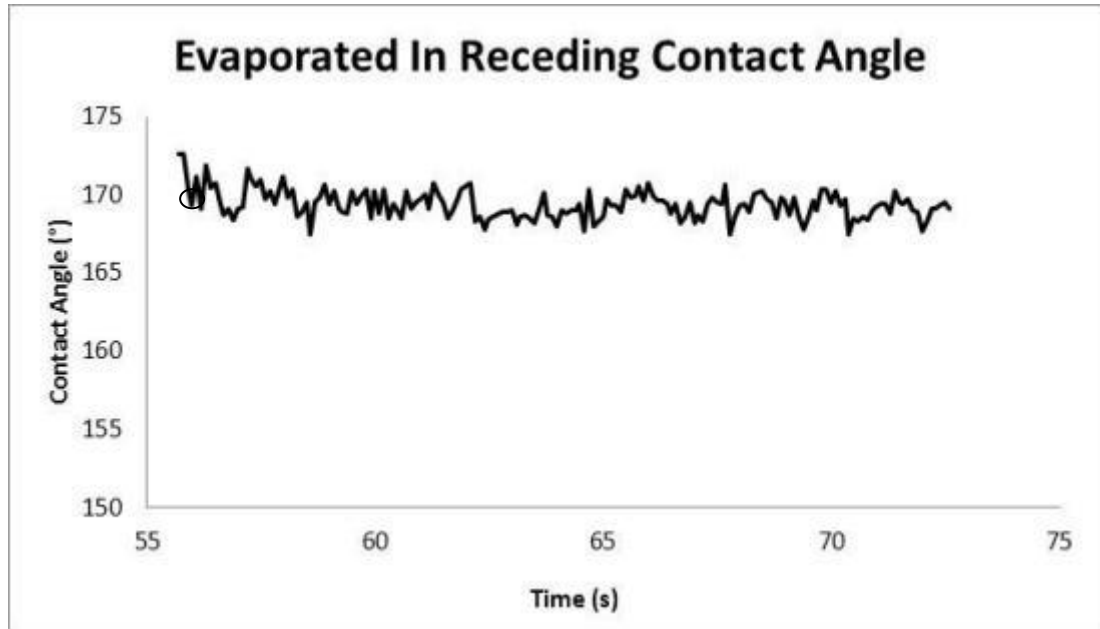


**Figure 4.17** shows contact angle measurements of a water droplet receding across the substrate

From the calculation of the advancing contact ( $\theta_a$ ) angle of  $175.9^\circ$  and receding ( $\theta_r$ ) of  $171.8^\circ$ , the contact angle hysteresis of the 20nm evaporated In layer on carbon spheres can thus be determined to be ( $\theta_a$ ) minus ( $\theta_r$ ), therefore contact angle hysteresis is equal to  $4.1^\circ$ . This result of hysteresis of  $4.1^\circ$  is in agreement with the sliding angle of  $3.5^\circ$  calculated for the same substrate.

#### 4.4 Self-Cleaning Properties

The demonstration of the self-cleaning ability of the material although simple, is effective in displaying the desired property of the material. A deposited layer of the superhydrophobic coating on a substrate is brought into contact with

water by either placing a droplet of water on the surface and allowing it to move freely on the surface with minimal tiling or by dropping water from several centimetres above the surface simulating rainfall and allowing the water to bounce off the surface and roll away. Contaminants such as carbon black or water soluble dyes in powder form can also be placed on the surface. When the water droplet comes in contact with these contaminants, they are picked up by the water droplet and removed from the surface demonstrating the self-cleaning characteristic of the material simply and effectively in an accessible manner.

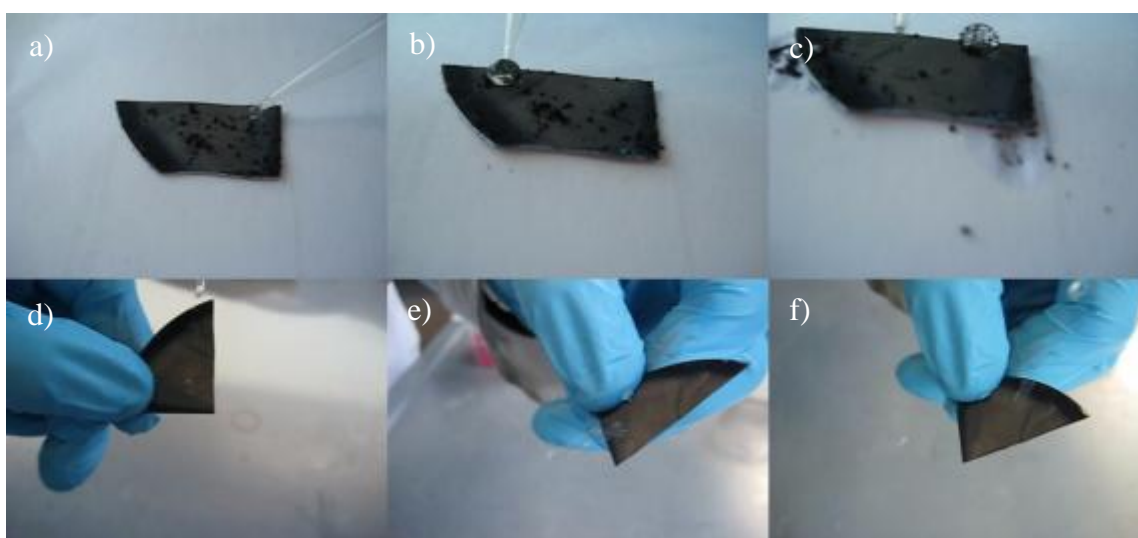


**Figure 4.18** Images a – c The ability of a drop of water to be easily moved on the surface of the self-cleaning material and the ability of the drop to remove carbon back from the surface, images d – f show the extreme hydrophobicity of the material with a drop of water falling from a syringe striking the surface and bouncing off.

Figure 4.18 shows the ability of 20nm In layer deposited on a film of carbon spheres to remove a contaminant such as carbon black from the surface of the substrate. It can be seen from Figure 4.18 c) that as the drop falls off the substrate the carbon black is deposited onto the underlying paper thereby demonstrating the ability of the



material to self-clean when in contact with water. No water is left on the substrate displaying the complete coverage of the substrate with the superhydrophobic coating. This is particularly evident in images Figure d – f where the drop of water bounces off the surface of the material without wetting the surface.

## 5. Conclusion

It was seen that through the optimisation of parameters during the synthesis of carbon spheres, the size and morphology of the particles could be controlled with the formation of roughly 1  $\mu\text{m}$  spheres produced on a consistent basis. The temperature control programme and volume of squalane injected prior to analysis were seen to give the most desirable size and morphology of particles produced. The use of selected metal precursors for thermal evaporation such as In displayed the desired characteristics of aspect ratio and island formation for the creation of nanosized asperities on the surface of the spheres large enough to support the bridging of water between them. This allowed the formation of a stable Cassie-Baxter wetting regime displaying superhydrophobic self-cleaning properties comparable with that seen in nature. Although all metal substrates used are of high surface energy In is the metal that displays dramatically increased contact angle. This increase in contact angle can be attributed to the nanoscale islands created on the surface of the carbon spheres. This island formation of In allows for the spaces between islands of In to support pockets of air between the asperities. This buffering In/air “composite” structure supports the impinging water droplet minimising contact between the droplet and the surface material. It is therefore the structure of the In as compared to the composition that has the greatest effect to increasing water contact angle as compared to the other evaporated metals as all metals have similar hydrophilic wetting on flat surfaces. It was shown through the use of evaporated In on carbon spheres that a water contact angle of  $\sim 170^\circ$  with low contact angle hysteresis of below  $10^\circ$  was capable of being produced in a repeatable process. The as-prepared surface displayed the ability to mimic that of the surface of the lotus leaf with the ability to remove contaminants

such as carbon black through the use of rolling droplets of water across its surface due to its superhydrophobicity.

## 6. Future Work

The use of high surface energy material for use as superhydrophobic materials is a relatively new concept in the formation of self-cleaning materials with the greatest interest in research seen in creation of a roughened surface with subsequent coating with low surface energy materials. Due to the large amount of research in this field varying materials and processes have been used to fabricate materials which mimic the superhydrophobicity of the lotus leaf. In order to compete with these materials in terms of optical properties such as transparency, the overall size of the carbon particles would have to be greatly reduced to approximately 50nm in diameter with a 20nm layer of evaporated In for a highly transparent film to be created according to the Fresnel Equation (Equation 4). With the use of other metal precursors that form islands on the surface of the carbon spheres, the refractive indices of the material could be matched for the formation of an antireflective material. While considering new materials to replace In as a surface coating of the spheres to produce superhydrophobic properties, some properties of the material should be considered. In order for large scale production of such a coating, the cost of the material will become a greater factor. In is a rare metal and thus expensive, therefore cheaper alternatives should be sought. The ability of the material to create islands of appropriate size on the surface of the carbon should be seen as a critical factor.

With what has been discovered throughout the course of this work, it has been displayed that with the use of inorganic materials and dual-scale hierarchical roughness, the possibility of creating lotus-like materials with superior superhydrophobicity and self-cleaning properties is possible without the inherent drawbacks of organic coatings. With the ever-growing demand for such a material, the potential applications are wide and varied and show that a material such as this

could produce a product which could have massive market potential. The key to producing a material to fit all applications will be one which can be tailored to purpose, durable, with high superhydrophobicity and low contact angle hysteresis. For this reason the work here displays a potential route towards the foremost self-cleaning coatings of the future.

## 7 References

1. Allyn Freeman, B.G., *Why Didn't I Think of That? Bizarre Origins of Ingenious Inventions We Couldn't Live Without*. John Wiley & Sons, 1997.
2. Gao, L. and T.J. McCarthy, *The "Lotus Effect" Explained: Two Reasons Why Two Length Scales of Topography Are Important*. Langmuir, 2006. **22**(7): p. 2966-7.
3. Young, T., *An essay on the cohesion of fluids*. Philosophical Transactions of the Royal Society of London, 1805. **95**: p. 65-87.
4. Woodward, J.T., H. Gwin, and D.K. Schwartz, *Contact Angles on Surfaces with Mesoscopic Chemical Heterogeneity*. Langmuir, 2000. **16**(6): p. 2957-61.
5. Sun, T., W. Song, and L. Jiang, *Control over the responsive wettability of poly(N-isopropylacrylamide) film in a large extent by introducing an irresponsive molecule*. Chemical Communications, 2005(13): p. 1723-5.
6. Nishino, T., et al., *The Lowest Surface Free Energy Based on  $-CF_3$  Alignment*. Langmuir, 1999. **15**(13): p. 4321-3.
7. Wenzel, R.N., *Resistance of Solid Surfaces to wetting by Water*. Industrial & Engineering Chemistry, 1936. **28**(8): p. 988-94.
8. Cassie, A.B.D. and S. Baxter, *Wettability of porous surfaces*. Transactions of the Faraday Society, 1944. **40**: p. 546-51.
9. Yoshimitsu, Z., et al., *Effects of Surface Structure on the Hydrophobicity and Sliding Behavior of Water Droplets*. Langmuir, 2002. **18**(15): p. 5818-22.
10. Lin, J., et al., *Fabrication of biomimetic superhydrophobic surfaces inspired by lotus leaf and silver ragwort leaf*. Nanoscale, 2011. **3**(3): p. 1258-62.

11. Feng, L., et al., *Petal Effect: A Superhydrophobic State with High Adhesive Force*. Langmuir, 2008. **24**(8): p. 4114-9.
12. Quéré, D. and M. Reyssat, *Non-adhesive lotus and other hydrophobic materials*. Philosophical Transactions of the Royal Society A: Mathematical, Physical and Engineering Sciences, 2008. **366**(1870): p. 1539-56.
13. Pease, D.C., *The Significance of the Contact Angle in Relation to the Solid Surface*. The Journal of Physical Chemistry, 1945. **49**(2): p. 107-10.
14. Bartell, F.E. and J.W. Shepard, *Surface Roughness as Related to Hysteresis of Contact Angles. II. The Systems Paraffin–3 Molar Calcium Chloride Solution–Air and Paraffin–Glycerol–Air*. The Journal of Physical Chemistry, 1953. **57**(4): p. 455-8.
15. Chen, W., et al., *Ultrasuperhydrophobic and ultrasuperoleophobic surfaces: some comments and examples*. Langmuir, 1999. **15**(10): p. 3395-9.
16. Youngblood, J.P. and T.J. McCarthy, *Ultrasuperhydrophobic Polymer Surfaces Prepared by Simultaneous Ablation of Polypropylene and Sputtering of Poly(tetrafluoroethylene) Using Radio Frequency Plasma*. Macromolecules, 1999. **32**(20): p. 6800-6.
17. Gao, L. and T.J. McCarthy, *How Wenzel and Cassie Were Wrong*. Langmuir, 2007. **23**(7): p. 3762-5.
18. Milne, A.J.B. and A. Amirfazli, *The Cassie equation: How it is meant to be used*. Advances in Colloid and Interface Science, 2012. **170**(1–2): p. 48-55.
19. Nosonovsky, M. and B. Bhushan, *Biologically Inspired Surfaces: Broadening the Scope of Roughness\*\**. Advanced Functional Materials, 2008. **18**(6): p. 843-55.

20. Liu, Y., X. Chen, and J.H. Xin, *Hydrophobic duck feathers and their simulation on textile substrates for water repellent treatment*. Bioinspiration & Biomimetics, 2008. **3**(4): p. 046007.
21. Dickinson, M., *How to walk on water*. Nature, 2003. **424**(6949): p. 621-2.
22. Hu, D.L., B. Chan, and J.W.M. Bush, *The hydrodynamics of water strider locomotion*. Nature, 2003. **424**(6949): p. 663-6.
23. Feng, X.-Q., et al., *Superior Water Repellency of Water Strider Legs with Hierarchical Structures: Experiments and Analysis*. Langmuir, 2007. **23**(9): p. 4892-6.
24. Gao, X. and L. Jiang, *Biophysics: Water-repellent legs of water striders*. Nature, 2004. **432**(7013): p. 36-.
25. Hosono, E., et al., *Superhydrophobic Perpendicular Nanopin Film by the Bottom-Up Process*. Journal of the American Chemical Society, 2005. **127**(39): p. 13458-9.
26. Liu, Y., D. Nolte, and L.J. Pyrak-Nolte, *Pinned Films and Capillary Hysteresis in Microfluidic Channels*. Lab on a Chip, 2012.
27. Zheng, Y., X. Gao, and L. Jiang, *Directional adhesion of superhydrophobic butterfly wings*. Soft Matter, 2007. **3**(2): p. 178-82.
28. Gao, L. and T.J. McCarthy, *Contact Angle Hysteresis Explained*. Langmuir, 2006. **22**(14): p. 6234-7.
29. Quere, D., *Surface chemistry: Fakir droplets*. Nat Mater, 2002. **1**(1): p. 14-5.
30. Roach, P., N.J. Shirtcliffe, and M.I. Newton, *Progress in superhydrophobic surface development*. Soft Matter, 2008. **4**(2): p. 224-40.



31. Wagner, T., C. Neinhuis, and W. Barthlott, *Wettability and contaminability of insect wings as a function of their surface sculptures*. *Acta Zoologica*, 1996. **77**(3): p. 213-25.
32. Neinhuis, C. and W. Barthlott, *Characterization and distribution of water-repellent, self-cleaning plant surfaces*. *Annals of Botany*, 1997. **79**(6): p. 667-77.
33. Mozumder, M.S., H. Zhang, and J. Zhu, *Mimicking Lotus Leaf: Development of Micro-Nanostructured Biomimetic Superhydrophobic Polymeric Surfaces by Ultrafine Powder Coating Technology*. *Macromolecular Materials and Engineering*, 2011.
34. Bhushan, B., C. Jung, and M. Nosonovsky, *Lotus Effect: Surfaces with Roughness-Induced Superhydrophobicity, Self-Cleaning, and Low Adhesion*. *Springer Handbook of Nanotechnology*, 2010. **3**: p. 1437-524.
35. Nosonovsky, M., et al., *Metal Matrix Composites for Sustainable Lotus-Effect Surfaces*. *Langmuir*, 2011. **27**(23): p. 14419-24.
36. Su, C., *A simple and cost-effective method for fabricating lotus-effect composite coatings*. *Journal of Coatings Technology and Research*, 2012: p. 1-7.
37. Zhan, N.Q., et al., *A novel multinozzle electrospinning process for preparing superhydrophobic PS films with controllable bead-on-string/microfiber morphology*. *Journal of Colloid and Interface Science*, 2010. **345**(2): p. 491-5.
38. Miyauchi, Y., B. Ding, and S. Shiratori, *Fabrication of a silver-ragwort-leaf-like super-hydrophobic micro/nanoporous fibrous mat surface by electrospinning*. *Nanotechnology*, 2006. **17**: p. 5151.

39. Cheng, Y.T., et al., *Effects of micro-and nano-structures on the self-cleaning behaviour of lotus leaves*. Nanotechnology, 2006. **17**: p. 1359.
40. Herminghaus, S., *Roughness-induced non-wetting*. EPL (Europhysics Letters), 2000. **52**: p. 165.
41. Wagner, P., et al., *Quantitative assessment to the structural basis of water repellency in natural and technical surfaces*. Journal of Experimental Botany, 2003. **54**(385): p. 1295-303.
42. F, B., *Nanotechnology in Coatings and Adhesive Applications*. Global Markets. BCC Research, NANO48A, 2010 January.
43. Mann, S., *Nanotechnology and Construction*. Nanoforum Report, 2006.
44. EasyJet, *easyJet tests nano technology for fuel efficiency*. 2011.
45. Rosencrantz, T., et al., *Increased solar energy and daylight utilisation using anti-reflective coatings in energy-efficient windows*. Solar Energy Materials and Solar Cells, 2005. **89**(2-3): p. 249-60.
46. Zhang, L., et al., *Layer-by-layer fabrication of broad-band superhydrophobic antireflection coatings in near-infrared region*. Journal of Colloid and Interface Science, 2008. **319**(1): p. 302-8.
47. Prevo, B.G., E.W. Hon, and O.D. Velev, *Assembly and characterization of colloid-based antireflective coatings on multicrystalline silicon solar cells*. Journal of Materials Chemistry, 2007. **17**(8): p. 791-9.
48. Yoldas, B.E. and T.W. O'Keeffe, *Antireflective coatings applied from metal-organic derived liquid precursors*. Appl. Opt., 1979. **18**(18): p. 3133-8.
49. Xu, D., et al., *Fabrication of raspberry SiO<sub>2</sub>/polystyrene particles and superhydrophobic particulate film with high adhesive force*. Journal of Materials Chemistry, 2012. **22**(12): p. 5784-91.

50. Kietzig, A.-M., S.G. Hatzikiriakos, and P. Englezos, *Patterned Superhydrophobic Metallic Surfaces*. Langmuir, 2009. **25**(8): p. 4821-7.
51. Feng, X., et al., *Reversible Super-hydrophobicity to Super-hydrophilicity Transition of Aligned ZnO Nanorod Films*. Journal of the American Chemical Society, 2003. **126**(1): p. 62-3.
52. Lim, J.-M., et al., *Superhydrophobic Films of Electrospun Fibers with Multiple-Scale Surface Morphology*. Langmuir, 2007. **23**(15): p. 7981-9.
53. Shiu, J.-Y., et al., *Fabrication of Tunable Superhydrophobic Surfaces by Nanosphere Lithography*. Chemistry of materials, 2004. **16**(4): p. 561-4.
54. Li, Y., et al., *Two-dimensional hierarchical porous silica film and its tunable superhydrophobicity*. Nanotechnology, 2006. **17**(1): p. 238.
55. Pozzato, A., et al., *Superhydrophobic surfaces fabricated by nanoimprint lithography*. Microelectronic Engineering, 2006. **83**(4–9): p. 884-8.
56. Cho, W.K., et al., *Water-repellent coating: formation of polymeric self-assembled monolayers on nanostructured surfaces*. Nanotechnology, 2007. **18**(39): p. 395602.
57. Khorasani, M.T., H. Mirzadeh, and Z. Kermani, *Wettability of porous polydimethylsiloxane surface: morphology study*. Applied Surface Science, 2005. **242**(3–4): p. 339-45.
58. Jin, M., et al., *Super-Hydrophobic PDMS Surface with Ultra-Low Adhesive Force*. Macromolecular Rapid Communications, 2005. **26**(22): p. 1805-9.
59. Cortese, B., et al., *Superhydrophobicity Due to the Hierarchical Scale Roughness of PDMS Surfaces*. Langmuir, 2008. **24**(6): p. 2712-8.

60. Burton, Z. and B. Bhushan, *Hydrophobicity, Adhesion, and Friction Properties of Nanopatterned Polymers and Scale Dependence for Micro- and Nanoelectromechanical Systems*. Nano Letters, 2005. **5**(8): p. 1607-13.
61. Casper, C.L., et al., *Controlling Surface Morphology of Electrospun Polystyrene Fibers: Effect of Humidity and Molecular Weight in the Electrospinning Process*. Macromolecules, 2003. **37**(2): p. 573-8.
62. Ma, M., et al., *Electrospun Poly(Styrene-block-dimethylsiloxane) Block Copolymer Fibers Exhibiting Superhydrophobicity*. Langmuir, 2005. **21**(12): p. 5549-54.
63. Ko, F., et al., *Electrospinning of Continuous Carbon Nanotube-Filled Nanofiber Yarns*. Advanced Materials, 2003. **15**(14): p. 1161-5.
64. Larsen, G., et al., *A Method for Making Inorganic and Hybrid (Organic/Inorganic) Fibers and Vesicles with Diameters in the Submicrometer and Micrometer Range via Sol–Gel Chemistry and Electrically Forced Liquid Jets*. Journal of the American Chemical Society, 2003. **125**(5): p. 1154-5.
65. Campbell, J.L., et al., *Electrowetting of Superhydrophobic ZnO Nanorods*. Langmuir, 2008. **24**(9): p. 5091-8.
66. Sakai, M., et al., *Sliding of Water Droplets on the Superhydrophobic Surface with ZnO Nanorods†† Part of the “Langmuir 25th Year: Wetting and superhydrophobicity” special issue*. Langmuir, 2009. **25**(24): p. 14182-6.
67. Wu, T., Y. Pan, and L. Li, *Study on superhydrophobic hybrids fabricated from multiwalled carbon nanotubes and stearic acid*. Journal of Colloid and Interface Science, 2010. **348**(1): p. 265-70.

68. Öner, D. and T.J. McCarthy, *Ultrahydrophobic Surfaces. Effects of Topography Length Scales on Wettability*. Langmuir, 2000. **16**(20): p. 7777-82.
69. del Campo, A., C. Greiner, and E. Arzt, *Contact Shape Controls Adhesion of Bioinspired Fibrillar Surfaces*. Langmuir, 2007. **23**(20): p. 10235-43.
70. Qian, B. and Z. Shen, *Fabrication of Superhydrophobic Surfaces by Dislocation-Selective Chemical Etching on Aluminum, Copper, and Zinc Substrates*. Langmuir, 2005. **21**(20): p. 9007-9.
71. Antonio Facchetti and T.J. Marks, *Front Matter*, in *Transparent Electronics*. 2010, John Wiley & Sons, Ltd. p. i-xxi.
72. Ohring, M., *The materials science of thin films; Deposition and Structure*. 2nd. Ed. ed. 2002, San Diego: Academic Press.
73. Lowndes, D.H., et al., *Synthesis of novel thin-film materials by pulsed laser deposition*. Science, 1996. **273**(5277): p. 898-903.
74. Rossnagel, S. and J. Hopwood, *Metal ion deposition from ionized mangetron sputtering discharge*. Journal of Vacuum Science & Technology B: Microelectronics and Nanometer Structures, 1994. **12**(1): p. 449-53.
75. Thompson, D. and S. Johar, *Nonlinear sputtering effects in thin metal films*. Applied Physics Letters, 1979. **34**(5): p. 342-5.
76. Pierson, H.O., *Handbook of chemical vapor deposition [ie deposition](CVD): principles, technology, and applications*. 1999: William Andrew.
77. Bormashenko, E., et al., *Wetting Properties of the Multiscaled Nanostructured Polymer and Metallic Superhydrophobic Surfaces*. Langmuir, 2006. **22**(24): p. 9982-5.

78. Bormashenko, E., et al., *Superhydrophobic Metallic Surfaces and Their Wetting Properties*. Journal of Adhesion Science & Technology, 2008. **22**(3/4): p. 379-85.
79. Pacifico, J., et al., *Superhydrophobic effects of self-assembled monolayers on micropatterned surfaces: 3-D arrays mimicking the lotus leaf*. Langmuir, 2006. **22**(26): p. 11072-6.
80. Ofir, Y., et al., *Controlled fluorination of FePt nanoparticles: hydrophobic to superhydrophobic surfaces*. Advanced Materials, 2007. **19**(22): p. 4075-9.
81. Hou, L., et al., *Multiple-structured nanocrystals towards bifunctional photoluminescent-superhydrophobic surfaces*. J. Mater. Chem., 2010. **20**(19): p. 3863-8.
82. Yabu, H. and M. Shimomura, *Single-step fabrication of transparent superhydrophobic porous polymer films*. Chemistry of materials, 2005. **17**(21): p. 5231-4.
83. Chang, K.C., et al., *Preparation of super-hydrophobic film with fluorinated-copolymer*. Journal of applied polymer science, 2007. **104**(3): p. 1646-53.
84. Barrett, C.A., et al., *Complete Synthesis of Germanium Nanocrystal Encrusted Carbon Colloids in Supercritical CO<sub>2</sub> and their Superhydrophobic Properties*. Langmuir, 2011. **27**(17): p. 11166-73.
85. Míguez, H., et al., *Control of the Photonic Crystal Properties of fcc-Packed Submicrometer SiO<sub>2</sub> Spheres by Sintering*. Advanced Materials, 1998. **10**(6): p. 480-3.
86. Jiang, P., et al., *Template-Directed Preparation of Macroporous Polymers with Oriented and Crystalline Arrays of Voids*. Journal of the American Chemical Society, 1999. **121**(50): p. 11630-7.

87. Park, S.H. and Y. Xia, *Fabrication of Three-Dimensional Macroporous Membranes with Assemblies of Microspheres as Templates*. Chemistry of materials, 1998. **10**(7): p. 1745-7.
88. Mer, V.K.L., *Nucleation in Phase Transitions*. Industrial & Engineering Chemistry, 1952. **44**(6): p. 1270-7.
89. Stöber, W., A. Fink, and E. Bohn, *Controlled growth of monodisperse silica spheres in the micron size range*. Journal of Colloid and Interface Science, 1968. **26**(1): p. 62-9.
90. Arkhireeva, A. and J.N. Hay, *Synthesis of sub-200 nm silsesquioxane particles using a modified Stober sol-gel route*. Journal of Materials Chemistry, 2003. **13**(12): p. 3122-7.
91. Gupta, R.B., *Supercritical fluid technology for particle engineering*. Drugs and the Pharmaceutical Sciences, 2006. **159**: p. 53.
92. Hemingway, M.G., *Hydrogel Nanoparticles from Supercritical Technology for Pharmaceutical and Seismological Applications*. 2010.
93. Matsuyama, K., et al., *Environmentally Benign Formation of Polymeric Microspheres by Rapid Expansion of Supercritical Carbon Dioxide Solution with a Nonsolvent*. Environmental Science & Technology, 2001. **35**(20): p. 4149-55.
94. Shim, J.-J., M.Z. Yates, and K.P. Johnston, *Polymer Coatings by Rapid Expansion of Suspensions in Supercritical Carbon Dioxide*. Industrial & Engineering Chemistry Research, 1999. **38**(10): p. 3655-62.
95. Quirk, R.A., et al., *Supercritical fluid technologies and tissue engineering scaffolds*. Current Opinion in Solid State and Materials Science, 2004. **8**(3–4): p. 313-21.

96. Thies, J. and B.W. Müller, *Size controlled production of biodegradable microparticles with supercritical gases*. European Journal of Pharmaceutics and Biopharmaceutics, 1998. **45**(1): p. 67-74.
97. Zhang, Y., et al., *Recent progress of double-structural and functional materials with special wettability*. Journal of Materials Chemistry, 2012. **22**(3): p. 799-815.
98. Smith, R. and R. Pitrola, *Influence of casting substrate on the acid–base interaction energies of various polyesters*. Polymer, 2000. **41**(26): p. 9111-22.
99. Cai, K., et al., *Surface structure and composition of flat titanium thin films as a function of film thickness and evaporation rate*. Applied Surface Science, 2005. **250**(1–4): p. 252-67.